

Final report on heat management system



ENABLE·H2

ENABLING cryogEnic Hydrogen-based CO2-free air transport

Call identifier

H2020-MG-2016-2017/H2020-MG-2017-Two-Stages

Project start

01.09.2018

Project duration

51 months



Grant Agreement: 769241

Call identifier: H2020-MG-2016-2017/H2020-MG-2017-Two-Stages

Project full title: ENABLEH2 – ENABLING cryogEnic Hydrogen-based CO2-free air transport

ENABLEH2

D2.4 - Final report on heat management system

Deliverable lead beneficiary: GKN

Authors: Alexandre Capitao Patrao, Carlos Xisto, Isak Jonsson, Anders Lundblad

Abstract:

Hydrogen is a promising aviation fuel due to its CO₂-free combustion and excellent cooling properties, which can be utilized in an aero engine for transferring heat to improve engine performance. This includes intercooling and recuperation, of which the former aims at decreasing NO_x emissions, compression work, increasing core specific power, and allowing for higher engine pressure ratios, while the latter allows for capturing waste heat in the engine exhaust which improves engine efficiency.

This report investigates the use of existing aerodynamic surfaces in the low-pressure compressor (LPC) and turbine rear structure (TRS) for the purpose of heat transfer. It also studies the conceptual design and integration of compact heat exchangers for intercooling and recuperation. System models for a baseline aircraft and hydrogen turbofan engine are set up, which allow for the calculation of fuel consumption and mission fuel burn but also provide engine data for more detailed aerothermal analysis and design of various heat management systems.

The use of existing aerodynamic surfaces for heat transfer can be carried out without incurring any additional pressure loss penalties, albeit for relatively low heat flows. Employing different combinations of stator surfaces for intercooling in a modern LPC design achieved at most a core air temperature drop in the order of 7 K. Even smaller core air temperature drops were found when using the TRS vane for heat transfer. Both cases highlighted the need for more surface area to achieve higher heat flows.

Compact heat exchangers, such as the finned tube type, can provide large heat flows with low to moderate pressure drops as long as the throughflow velocities on the air side are low, which means it is of critical importance to design a low-loss diffusing duct. Therefore, a large aerodynamic optimization campaign by means of CFD simulations is carried out to optimize a diffuser duct in conjunction with a heat exchanger and a contraction for different area ratios. It is observed that optimized designs could deliver an order of magnitude higher heat flows than existing aerodynamic surfaces with total pressure losses ranging from 4% to 7%.

A down-selection was carried out using full engine system level and conceptual design models to determine the most relevant concepts for further technology maturation studies. The baseline engine model was extended to include intercooling and recuperation by using pressure drop correlations from aerodynamically optimized duct designs. Several different engine configurations were created which used heat exchangers of different area ratios and combinations of intercooling and recuperation. The largest benefit in terms of SFC was seen for the recuperated and the intercooled recuperated configurations which decreased SFC by 4.6-6% depending on the operating point. The latter configuration also benefitted from a decrease of NO_x emissions (EINO_x) of 17% during cruise and 39% during take-off. Intercooled configurations reached decreases in SFC ranging from 1.5% to 3.4% and NO_x emissions from 12% to 40%. Fuel burn for the design mission of 3000 NM was reduced by approximately 5% for the recuperated and intercooled-recuperated engines.

The intercooled-recuperated concept using compact heat exchangers is finally the down-selected configuration as it is the highest performing from an aerothermal and system perspective. In addition to substantial fuel burn benefit, it achieves reduced core temperatures and the intercooler will also preheat the hydrogen which avoids icing in the recuperator. It should be highlighted that this configuration also offers both increases in thermal efficiency and decreases in NO_x emissions.

Table of Contents

1	Glossary	3
2	Introduction	4
3	Baseline hydrogen engine and aircraft	6
3.1	Engine design, performance and system model	6
3.2	Aircraft trade-factors	8
3.2.1	Application of trade-factors	11
4	Relevant heat transfer systems and their performance	12
4.1	Intercooling	12
4.1.1	Using existing aero surfaces for heat transfer	12
4.1.2	CFD methodology	13
4.1.3	Heat transfer on the ICD	13
4.1.4	Heat transfer on S2	15
4.1.5	Heat transfer on all stators	17
4.1.6	Conjugated ICD simulations	18
4.1.7	Effect of transition on cryogenic cooling	20
4.1.8	Conclusions on intercooling using existing aero surfaces	21
4.2	Recuperation	24
4.2.1	Heat transfer on the baseline TRS vane	25
4.2.2	Heat transfer on the high-aspect ratio TRS	26
4.2.3	Heat transfer on fully turbulent high-aspect ratio TRS	28
4.2.4	Comparison between the different TRS geometries and heat transfer potential for LH2	29
4.3	Compact heat exchanger design and integration	31
4.3.1	Compact heat exchangers	31
4.3.2	The ϵ -NTU method	33
4.3.3	Thermophysical properties	36
4.3.4	ICD heat exchanger designs for area ratio 4 and 6	36
4.3.5	Duct shape optimization	37
4.3.6	Pressure loss correlations	44
4.3.7	TRS heat exchanger conceptual design	47
5	Integrated performance and engine conceptual design	49
5.1	Integrated performance	49
5.1.1	Intercooled engines	49
5.1.2	Intercooled-recuperated and recuperated engines	50
5.2	Conceptual design and impact on fuel burn	51
6	Conclusions	55
7	References	57

1 Glossary

Abbreviation	Description
ACARE	Advisory Council for Aeronautics Research in Europe
AR	Area Ratio
BC	Boundary Condition
BPR	Bypass-Ratio
BWB	Blended Wing Body
CFD	Computational Fluid Dynamics
CO	Carbon Monoxide
CO ₂	Carbon Dioxide
FB	Fuel Burn
FPR	Fan Pressure Ratio
GA	Genetic Algorithm
GHG	Greenhouse Gas
HEX	Heat Exchanger
HPC	High Pressure Compressor
HPT	High Pressure Turbine
HTC	Heat Transfer Coefficient
HTR	Hub-to-Tip ratio
HWB	Hybrid Wing Body
ICD	Interconnecting Compressor Duct
IGV	Inlet Guide Vane
ISA	International Standard Atmosphere
LH ₂	Liquid Hydrogen
LHS	Latin Hypercube Sampling
LPT	Low Pressure Turbine
NIST	National Institute of Standards and Technology
NO _x	Nitrous Oxides
NTU	Heat exchanger Number of Transfer Units
Nu	Nusselt number
OPR	Overall Pressure Ratio
PAX	Passengers
PS	Pressure Side
Q	Heat flow
R1	Rotor 1 in the ENABLEH2 compressor
R2	Rotor 2 in the ENABLEH2 compressor
RBF	Radial Basis Functions
Re	Reynolds number
S1	Stator 1 in the ENABLEH2 compressor
S2	Stator 2/outlet guide vane in the ENABLEH2 compressor
SFC	Specific Fuel Consumption
SMR	Short-to-Medium Range
SS	Suction Side
T&W	Tube and Wing
TO	Take-Off
ToC	Top of Climb
TRS	Turbine Rear Structure
VINK	Virtual Integrated Compressor Demonstrator
WEICO	Chalmers in-house conceptual design tool

2 Introduction

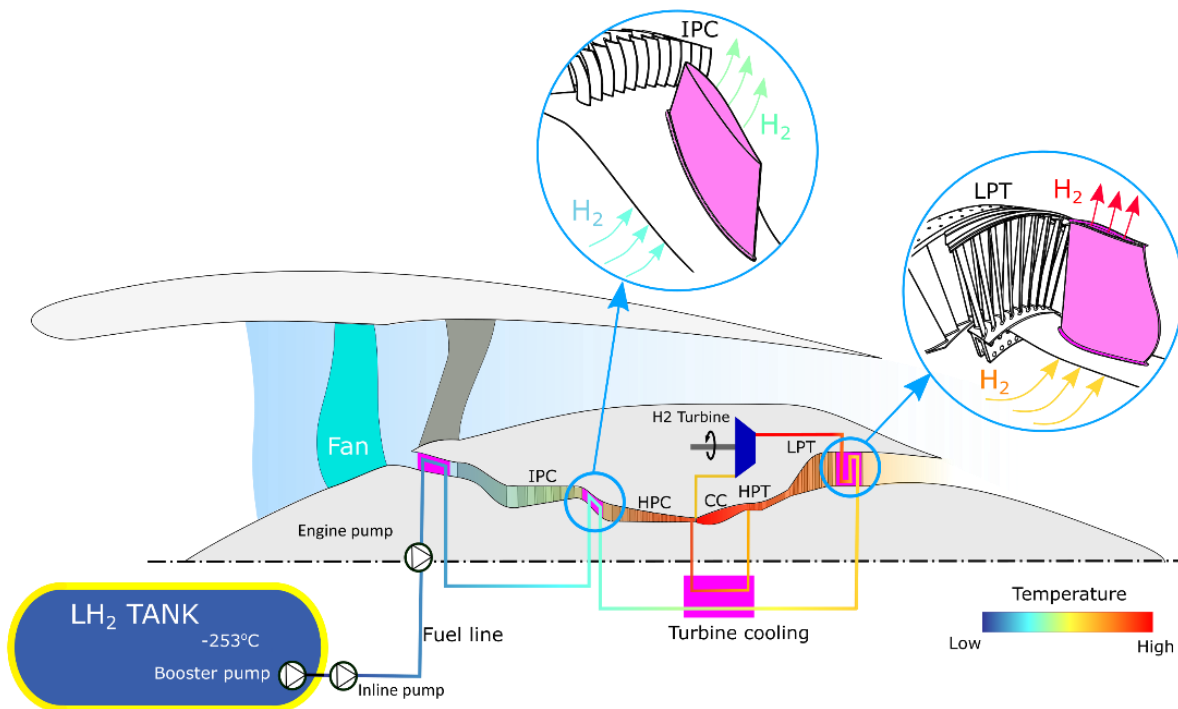


Figure 1 - Cross sectional meridional view of a turbofan engine in which different locations for core cooling using liquid hydrogen are shown. The used fuel, LH₂ (liquid hydrogen), is stored at its boiling point in the fuel tank. The LH₂ temperature is progressively increased due to the fuel flow across the different core installed heat exchangers [10].

Since the publishing of the European Green Deal in December 2019, the European Union (EU) has had the goal of achieving zero net emissions by 2050 as well as reducing Greenhouse Gas (GHG) emissions by at least 55% by 2030, compared to 1990 levels [1]. To achieve this challenging goal, emissions need to be reduced through all European industries. The largest potential reductions in CO₂ emissions in the EU lies in the transport and electricity production sectors, with reductions corresponding to 31% and 30% of total CO₂ emissions [2]. For aviation, the share amounts to 3.8% of total CO₂ emissions in the EU, collectively, and 13.9% of GHG emissions from transports [3]. Beyond CO₂ emissions there are additional emissions which are at least as important and impactful on the climate as CO₂, namely nitrogen oxides, water vapor contrails, sulphates, and soot particles [4]. The forementioned factors together with a continuously growing air traffic leads to the risk of tripling emissions by 2050 compared to 2015 [5].

In the case of the aviation industry, emission targets have been established by the ACARE (Advisory Council for Aeronautics Research in Europe) which stated that a 75% and 90% reduction in CO₂ and NO_x emissions, respectively, should be achieved by 2050 [6], therefore requiring the development and operational introduction of new technology and carbon-free fuels. The fuel that stands out as the most suitable option for aviation is liquid hydrogen (LH₂), due to the following advantages:

- CO₂-free combustion
- Higher specific energy compared to kerosene (2.8 times higher [7]).
- Elimination of CO₂, CO, soot, sulphur, and unburnt hydrocarbons emissions.
- Formidable coolant due to its high specific heat capacity.

The main disadvantages of LH₂ are:

- Lower density compared to kerosene
- Required cryogenic storage temperature, which affects propellant feed system size, mass, and insulation requirements.

The combination of high specific heat capacity and cryogenic storage temperature leads to interesting possibilities regarding engine thermal management, which is the process by which the fuel absorbs the heat generated by the different components and systems of the engine as it passes through them [8].

An example of this is shown in Figure 1 which shows a turbofan engine featuring precooling, intercooling, and recuperation. The precooler and intercooler deliver air with increased density, thus decreasing compression work. Moreover, their installation also allows for increasing overall pressure ratio (OPR) and core specific power without exceeding any cycle temperature limit. Another possible advantage arising for both pre- and intercooling is the possibility of reducing the combustor inlet temperature for a given OPR, which will curb NO_x emissions. For recuperation the waste heat in the engine exhaust can be recovered and used to either preheat the LH₂ before combustion or to drive an expander cycle turbine.

Several approaches for heat transfer exist in an aero engine. This report aims at investigating the potential for heat transfer in existing aerodynamic surfaces in the engine core but also the design of compact heat exchangers for intercooling and recuperation.

3 Baseline hydrogen engine and aircraft

The baseline engine and aircraft are developed in connection with the activities reported in deliverable D1.3 - LH2 T&W and BWB/HWB aircraft platform models. An illustration of the aircraft model is shown in Figure 2. The selection of the low-risk configuration for the reported optimization results is because Chalmers owns the aircraft model. Hence, we can easily generate non-linear trade factors that account for the effect of specific fuel consumption, engine weight and fan diameter into the aircraft mission fuel burn. This allows the creation of a more informed engine integration model that accounts for installation effects on the actual calculated aircraft performance.

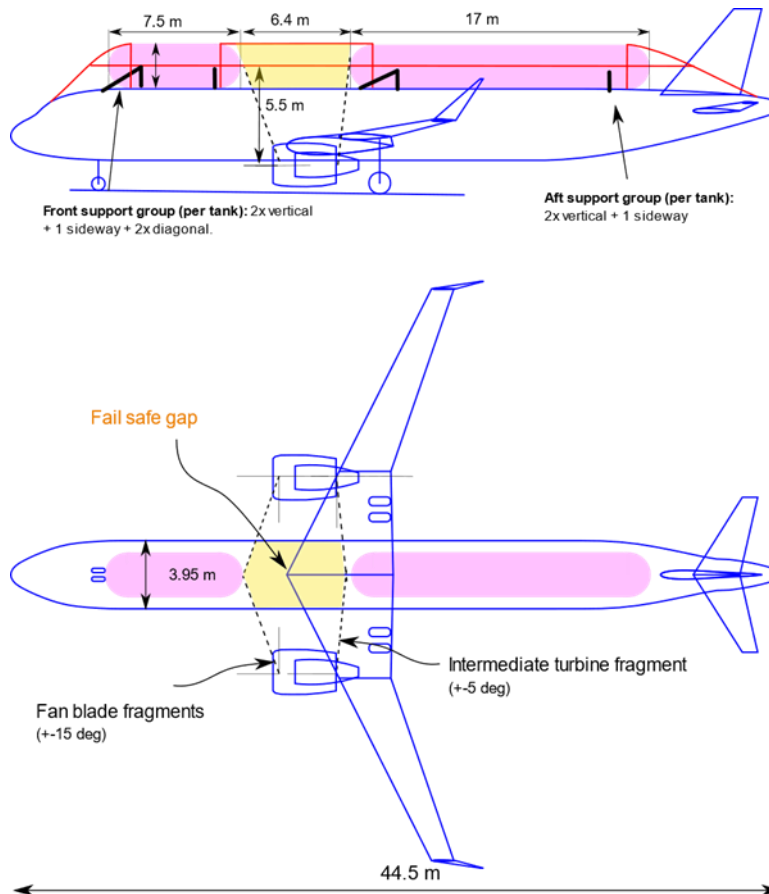


Figure 2 - Low-risk short-medium range aircraft with PVC insulated tanks mounted above the pressurized fuselage.

3.1 Engine design, performance and system model

The baseline hydrogen engine is a 30klbf thrust class, year 2050, geared turbofan engine for SMR applications. The engine does not feature a dedicated fuel heat management system (i.e. the fuel is pumped directly from the tank to the hydrogen combustor). The engine performance is derived using the technology parameters listed in Table 1, and is listed in Table 2. The thrust requirements are extracted from the baseline aircraft model early described in D1.3, and the initial estimates of fan pressure ratio and BPR are derived using rough estimates of the contribution of engine weight and drag on the nominal performance of the aircraft. It is noted that these are only early estimates for the low-pressure system performance that will later be corrected using aircraft derived linear-trade factors. The engine conceptual design was carried out using Chalmers' in-house tool WEICO (Weight and cost). A cross-sectional drawing is shown in Figure 4. The engine includes a three-stage low-pressure compressor, a 10-stage high-pressure compressor (HPC), a two-stage high-pressure turbine and a three-stage low-pressure turbine. The fan tip diameter at the inlet is 2.04 m, and the last stage blade height of the high-pressure compressor is 12 mm. Corrections to the polytropic efficiency with the last stage blade height are applied using the function shown in Figure 3 [9].

$$\eta_{p,HPC} = \eta_{p,0,HPC} + \Pi \left(0.0532 - \frac{0.5547}{\lambda} - \frac{1.7724}{\lambda^2} \right) \quad (1)$$

where λ is the last blade height in mm and Π is a correction factor assumed to be equal to 1 for the HPC and 0.5 for the HPT. For calculating the last blade height it is assumed an HPC exit hub-to-tip ratio of 0.92 and axial Mach number of 0.27. The correlation is used for every HPC design generated in the optimization loop.

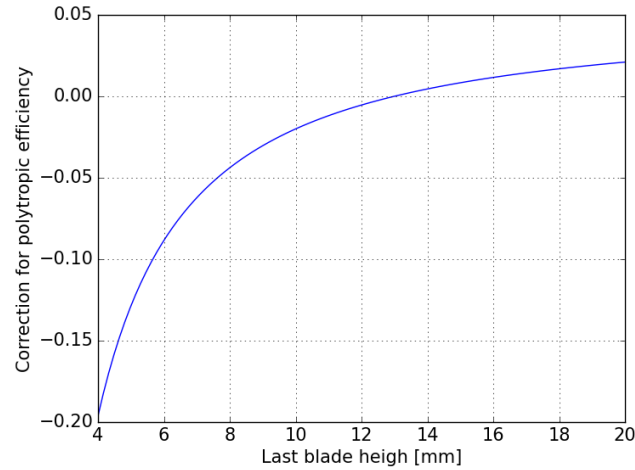


Figure 3 - HPC polytropic efficiency correction with last stage blade height

In Table 2 EINO_x is estimated for a micromix combustor using the correlation for dry air derived in the ENABLEH2 project:

$$\text{EINO}_x = 0.0864 \times P_3^{0.4} \times e^{T^3/191} \times \phi^{1.95} \quad [\text{g/kg fuel}]$$

The baseline interconnecting compressor duct (ICD) is shown in Figure 5 to establish the corner points required to conceptually design the intercooler. The intercooler diffuser, heat-exchanger and contraction duct will be later placed between the corner points that define ICD inlet and outlet.

Table 1 – 2050 performance data assumptions as per D1.1 – Common technical basis, given for cruise and ISA conditions unless stated otherwise.

2050 SMR	
Fan efficiency (outer fan, isentropic)	94.0%
FPR (outer fan)	1.45
Booster efficiency (polytropic)	92.0%
Cooling ratio (all points)	0.10
BPR (estimate, to be computed from optimization)	15.0
HPC efficiency (polytropic, subject to size correction)	92.0%
HPT Efficiency (isentropic)	91.0%
LPT efficiency (isentropic)	94.0%
OPR (top of climb)	50
T4 [K] (ISA, take-off)	1825

Table 2 – Performance data for the baseline LH2 SMR 2050 engine

	MTO	MCL	Mid-Cruise
Altitude (ft)	0	35000	35000
Mach Number	0	0.75	0.75
Net Thrust (lbs)	30,600	6,290	5,050
DT_{ISA} (K)	0	0	0
T3 (K)	871	795	758
P3 (bar)	41.0	17.4	14.7
T4 (K)	1825	1694	1603
BPR	17.1	16.7	18.2
FPR	1.44	1.54	1.45
OPR	40.5	50.2	42.3
T_{fuel} (K)	26.7	26.9	27.0
SFC (mg/Ns)	2.35	4.61	4.59
EINOx (g/kg fuel)	40.2	15.8	9.6
Fan diameter (m)	2.04		
Engine weight, including nacelle (kg)	3185		

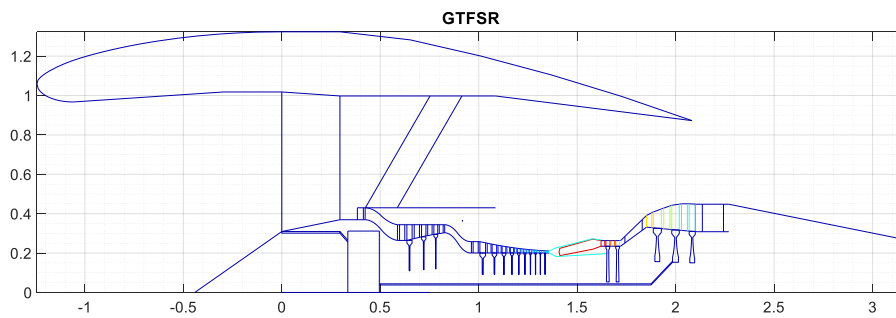


Figure 4 - Schematic engine layout for Y2050 SMR baseline concept

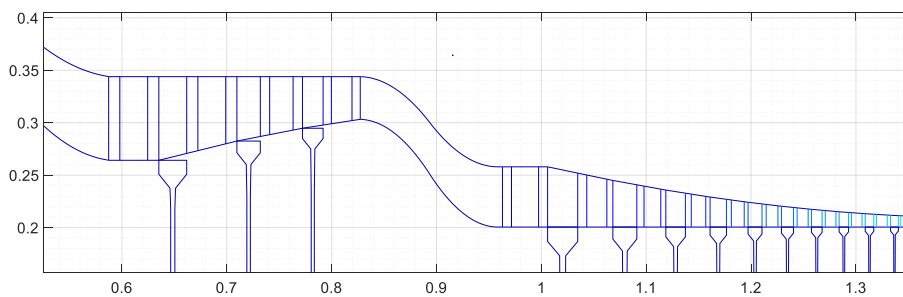


Figure 5 –Corner points defining the baseline ICD duct used as boundary conditions for the preliminary aerodynamic design of the intercooler.

3.2 Aircraft trade-factors

In order to properly account for the integrated effects of the new propulsion units on mission fuel burn, a set of linear trade-factors was created for the 2050 LH2 SMR aircraft, for which detailed performance is provided in deliverable 1.3. The mission characteristics and flight profile are tabulated in Table 3 and Table 4, respectively. It is noted that in order to properly model the aircraft design response for the

variation of engine performance parameters, engine and nacelle scalability with thrust was included in the present model, in terms of size and weight. After, important parameters relating to engine specific thrust and specific fuel consumption were independently varied to determine the linear response of the aircraft model in design and off-design conditions.

Table 3: SMR range aircraft mission characteristics.

Mission Characteristics	
Design Range	3000 NM
Economic range	900 NM
PAX (design)	200
Payload	21 000 kg
Cruise Mach	0.75
Climb Mach	0.75
Initial cruise altitude	35 000 ft

Table 4: Flight Profile

Flight profile		
Initial climb up to 10,000 ft	250 CAS	
Climb (ISA) after 10,000 ft	300 CAS	M0.75
Cruise (ISA)	M0.75	M0.75
Descent (ISA)	300 CAS	M0.75
Contingency	5% Trip Fuel	
Diversion	100 NM	25 000 ft
Hold	30 min	1500 ft

The resulting linear trade-factors are listed in Table 6. The variation is given relative to the design point conditions:

Table 5 – Reference engine design and performance characteristics

Engine Characteristics	
Fan diameter reference [m]	2.04
SFC reference, max cruise @M0.75, 35,000ft. [mg/Ns]	4.6
Reference engine mass [kg]	3185

Table 6 – Trade-factors derived for the year 2050 LH2 SMR aircraft.

	Economic (900NM)	Design (3000NM)
SFC -2%	-2.5% FB**	-2.66% FB**
Weight (inc. nacelle)* +500kg	+2.44% FB**	+2.58% FB**
Fan diameter*** +2%	+0.15% FB**	+0.16% FB**

* Weight is for a single power plant

** Trip fuel burn, not including taxi

*** Mainly impacts on nacelle drag

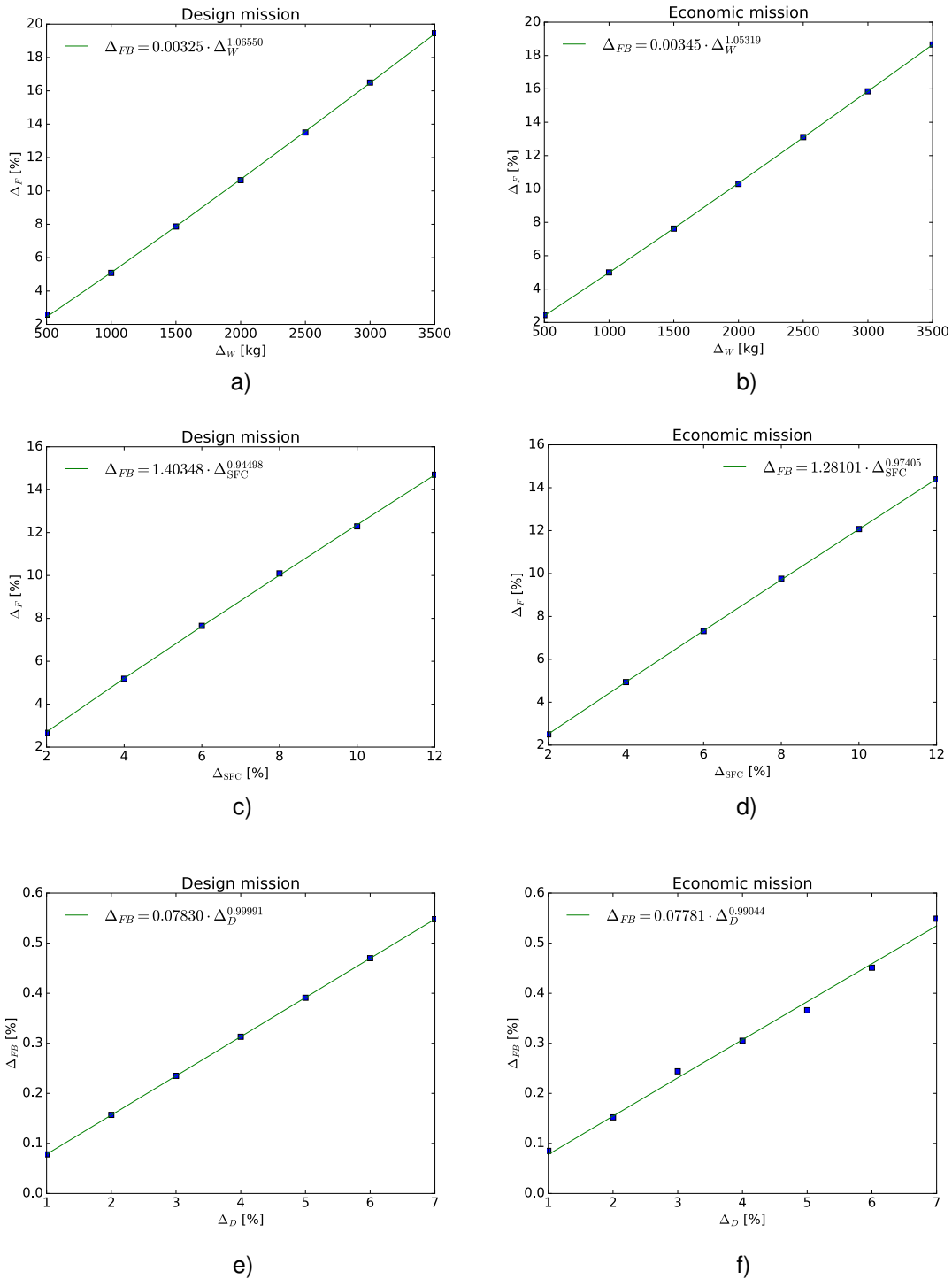


Figure 6 – Aircraft fuel burn trade factors accounting for the impact of: (per) engine mass increase (kg) in the design (a) and economic mission (b) increase in fuel burn (%). SFC reduction (%) in the reduction of fuel burn (%) in the design (c) and economic mission (d). Fan diameter increase (%) in fuel burn increase for the design (e) and economic (f) mission. It is noted that the increase in fan diameter is only credited with respect to increases in drag coefficient, the impact of fan size in weight is addressed separately in the weight trade factor.

3.2.1 Application of trade-factors

The computed trade-factors reflect the impact of the engine specific parameters on the whole aircraft fuel burn performance (fuel quantity is scaled to ensure that the mission range/payload is satisfied). For example, looking into Table 6, one can derive that a 1% reduction in SFC returns a 1.25% reduction in fuel burn for the economic, 900 NM, missions. Reduction in specific fuel consumption, reduces the requirement in terms of hydrogen tank weight, weight structures, wing size, etc. The following equations are generally applicable for the SMR aircraft, for parameter ranges given in Figure 6, but the linearity shown seems to allow for an applicability for a wider range variation. The total fuel burn variation relative to the design point conditions given above (Table 3 - Table 5) can be calculated as follows.

$$\Delta_{FB,total} = \left(1 + \frac{\Delta_{FB,W}}{100}\right) \left(1 + \frac{\Delta_{FB,D}}{100}\right) \left(1 - \frac{\Delta_{FB,SFC}}{100}\right) - 1$$

Where the relative SFC contribution can be estimated using the following correlation.

$$\Delta_{FB,SFC} = 1.40348 \cdot \Delta_{SFC}^{0.94498} \text{ (Design mission, 3000 NM)}$$

$$\Delta_{FB,SFC} = 1.28101 \cdot \Delta_{SFC}^{0.97405} \text{ (Economic mission, 900 NM)}$$

$$\Delta_{SFC} = \left(1 - \frac{SFC}{SFC_{ref}}\right) \cdot 100$$

The engine mass (kg) contribution can be estimated using:

$$\Delta_{FB,W} = 0.00325 \cdot \Delta_W^{1.06550} \text{ (Design mission, 3000 NM)}$$

$$\Delta_{FB,W} = 0.00345 \cdot \Delta_W^{1.05319} \text{ (Economic mission, 900 NM)}$$

$$\Delta_W = (W - W_{ref}) \text{ [kg]}$$

The relative fan diameter contribution to total fuel burn:

$$\Delta_{FB,D} = 0.07830 \cdot \Delta_D^1 \text{ (Design mission, 3000 NM)}$$

$$\Delta_{FB,D} = 0.07781 \cdot \Delta_D^{0.99044} \text{ (Economic mission, 900 NM)}$$

$$\Delta_D = \left(\frac{D}{D_{ref}} - 1\right) \cdot 100$$

4 Relevant heat transfer systems and their performance

The present chapter investigates the conceptual design and performance of relevant engine core heat-sinks. It is divided into a section on intercooling, one on recuperation, and one on compact heat exchangers. The first two sections analyze the use of existing turbomachinery surfaces for the purpose of heat transfer while the last section focuses on the design and integration of compact heat exchangers into the core air stream.

4.1 Intercooling

For the present report, intercooling refers to cooling of the core air, using cryogenic LH2 at an intermediate compression station (between the low-pressure and high-pressure compressors). Intercooling is used to increase the fuel enthalpy before combustion and allows for an increase in core specific work at a given thrust and HPC discharge temperature constraint. The present section evaluates the aerothermal performance of different intercooler concepts by numerically investigating the feasibility of existing turbomachinery surfaces for heat transfer.

4.1.1 Using existing aero surfaces for heat transfer

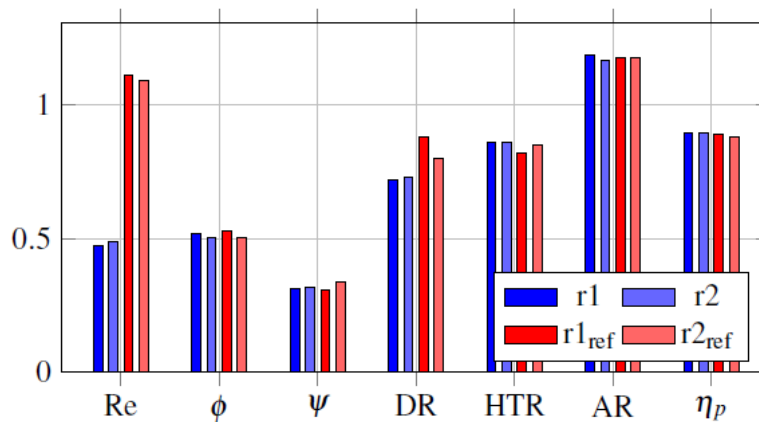


Figure 7 - ENABLEH2 compressor parameters in comparison to reference engine (VINK) parameters. AR – Aspect ratio; HTR - Hub-to-tip ratio; DR – Degree of reaction; Re – Chord based Reynolds number, divided by 10^6 ; ϕ – Flow coefficient; ψ – Stage loading; η_p – Polytropic efficiency. Image extracted from [12].

Using existing aero surfaces for heat transfer incurs no additional pressure loss since no additional wetted surface is added. This approach has been tested by means of CFD simulations of the 2.5 stage low-speed compressor described in [10] and [11] and which will be referred to here as the ENABLEH2 compressor. This compressor was designed to replicate the final stages of a modern high-speed LPC in the notional engine VINK [12] and will be used for experimental, computational, and validation purposes. The ENABLEH2 compressor is representative of a modern compressor (VINK) in terms of typical aerodynamic parameters such as flow coefficient, stage loading and degree of reaction, which are presented in Figure 7. The Reynolds and Mach numbers are lower for this compressor compared to the VINK notional engine as it constitutes a low-speed design for implementation in a test rig, implying that a larger amount of heat transfer should be obtainable from a high-speed design compared with the results presented in this section of the report. Nevertheless, the ENABLEH2 compressor constitutes a reasonable and conservative surrogate design for investigating the heat transfer performance of existing turbomachinery surfaces. Remaining compressor properties, design point operational conditions, and geometry are shown in Figure 8.

ENABLEH2 Compressor	
Rotational Speed	1920 rpm
Design corr. mass flow	18.4 kg/s
Pressure ratio	1.07
Tip Speed	100 m/s
Axial Velocity	70 m/s
Rotor Re_c	600 000
Avg Tip radius	620 mm
Avg Hub radius	540 mm
N. stator Blades (IGV, S1, S2, ICD)	75, 126, 124, 8
N. rotor Blades (R1, R2)	61, 69
Avg Aspect Ratio	2.157
Avg Tip Clearance	0.75 mm

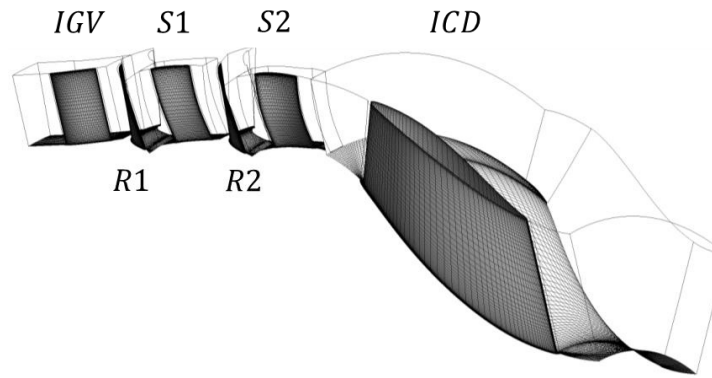


Figure 8 - **Left:** ENABLEH2 compressor properties and design operating point. **Right:** Compressor geometry, composed of an Inlet Guide Vane (IGV), Rotor 1 (R1), Stator 1 (S1), Rotor 2 (R2), Stator 2 (S2), and Interconnecting Compressor Duct (ICD)

4.1.2 CFD methodology

ANSYS Turbogrid was used to generate structured, hexahedral meshes (see Figure 8) of the different computational domains which constitutes the ENABLEH2 compressor. The first node height of the mesh was set below $y^+ = 1$ at the walls. The solver ANSYS CFX 2021r1 was used to simulate the flowfield, by solving the compressible flow Reynolds Averaged Navier-Stokes (RANS) equations together with the $k - \omega$ SST turbulence model. The working fluid was set as air perfect gas with temperature dependent thermal conductivity and viscosity, implemented as polynomials using data from NIST REFPROP [18]. The following boundary conditions were set:

- Inlet: Total pressure and temperature of 95275 Pa and 288.15 K. Specified on the IGV inlet. Turbulence intensity 5%.
- Outlet: Static pressure of 100102 Pa. This value is a result from a series of simulations where the outlet pressure was varied in order to obtain the correct design massflow.

The total pressure losses for each stator in the ENABLEH2 compressor at the design point are shown in Table 7 and will be compared with pressure losses for the cooled configurations in subsequent sections of this report.

Table 7 – Total pressure losses for each stator at the design point. The pressure losses have been normalized with the total pressure at the inlet of each respective stator domain.

	IGV	S1	S2	ICD
Total pressure loss:	0.063%	0.100%	0.157%	0.104%

4.1.3 Heat transfer on the ICD

The chosen approach for modelling the heat transfer from the air side to the hydrogen side consists of an overall heat transfer coefficient on the vane surfaces of the ENABLEH2 compressor rig. This heat transfer coefficient mimics the thermal resistance of an assumed generic cooling channel geometry underneath the vane surface. These channels are assumed to have a square cross-section with a side of 0.5 mm, and a spacing of 1.5 mm between each channel, and a 0.5 mm wall thickness for the side facing the core air flow. The channels are assumed to be aligned with the span direction of the stators and the number of channels is calculated using the midspan chord.

This boundary condition assumes that heat transfer through the stator surfaces can be approximated as one-dimensional. In this case the heat transfer can be treated as a thermal circuit and its thermal resistance (per unit area) can be calculated as follows:

$$R''_{tot} = \frac{1}{h_{conv,air}} + \frac{t}{k} + \frac{1}{h_{conv,LH2}} \quad (2)$$

Here it assumed that the thickness t of the wall between the channel and stator surface is 0.5 mm and the thermal conductivity of the vane is 120 [W/m K] (conservative for Alu alloys). The convective heat transfer of the hydrogen flow in the cooling channels is calculated using the following properties:

$$\begin{aligned}
 p &= 42 \text{ bar} \\
 T &= 100 \text{ K} \\
 \dot{m}_{LH2} &= 0.1840 \text{ kg/s} \\
 N_{channels_per_vane} &= 318 \\
 Re &= 32625 \\
 Nu &= 76.62 \\
 h_{conv,LH2} &= 13687 \text{ [W/m}^2\text{K]}
 \end{aligned} \tag{3}$$

The hydrogen massflow is calculated by setting a fuel-to-air mass ratio of 1%, which corresponds to ToC for the baseline hydrogen engine. In CFX the thermal resistance for the heat transfer occurring inside the vane itself can be used as a boundary condition in terms of an overall heat transfer coefficient U in an equation analogous to Newton's law of cooling (Eq. (4)). The LH2 bulk temperature is set as constant along the channel length due to the assumption that the heat transfer will be relatively low.

$$\begin{aligned}
 q_x'' &= U(T_{wall,air} - T_{LH2}) \\
 U &= \frac{1}{R_{tot}''} = 1 / \left(\frac{t}{k} + \frac{1}{h_{conv,LH2}} \right) = 12949 \text{ [W/m}^2\text{K]}
 \end{aligned} \tag{4}$$

$$T_{LH2} = 100 \text{ [K]}$$

This approach allows for modelling the heat transfer occurring inside the vane without explicitly designing and simulating the entire cooling channel geometry in a conjugate CFD simulation. The 100 K is chosen for maximizing the temperature difference between air and hydrogen while avoiding condensation of nitrogen and oxygen in the core air. This temperature will require some preheating of the hydrogen, possible electrically heated or through recirculation of warm, downstream hydrogen since pressurizing the hydrogen from tank conditions (~21 K, 1.6 bar) to 42 bar only increases the hydrogen bulk temperature by a few degrees (4 K for pump with 75% efficiency). Nevertheless, this boundary condition was included in the CFD model in section 4.1.2 and run at an outlet pressure which would result in the design corrected mass flow (18.4 kg/s) of the uncooled, original CFD model.

Table 8 – Overall results for the cryogenic ICD simulation

ICD cooling	
Corrected mass flow [kg/s]	18.41
Q ICD vane [kW]	20.53
Equivalent core air temperature drop ΔT_0 [K]	1.18
Vane surface area [m ²]	0.448
Ave. heat transfer coeff. ICD vane [W/m ² K]	240.1

Table 9 – Total pressure losses for each stator for the cryogenic ICD simulation. The pressure losses have been normalized with the total pressure at the inlet of each respective stator domain.

	IGV	S1	S2	ICD
Total pressure loss:	0.063%	0.100%	0.157%	0.101%

The results from this simulation have been summarized in Table 8 and shows that a heat flow of 20.53 kW ($\Delta T_0 = -1.18$ K) for a full ICD annulus is obtainable using this setup. Table 9 lists the pressure losses across the different static components of the compressor. It can also be seen that corrected mass flow is slightly higher than during the design point which is due to a lower pressure drop in the ICD compared to the design point performance (Table 7). Wall temperature and heat flux is included in Figure 9 and Figure 10 shows very low wall temperatures on the ICD vane, which is indicative of high thermal resistance on the air side. This is also evident when calculating the thermal resistances for the core air, conduction in the vane, and LH2 cooling channels, as can be seen in Eq. (5). The large magnitude of the air side thermal resistance means that the overall heat transfer coefficient U is

dominated by the air side heat transfer and is relatively insensitive to changes in the hydrogen heat transfer coefficient.

$$R''_{tot} = R_{conv,air} + R_{cond} + R_{conv,LH2} = \frac{1}{h_{conv,air}} + \frac{t}{k} + \frac{1}{h_{conv,LH2}}$$

$$R_{conv,air} = 4.17 \cdot 10^{-3} \text{ [m}^2\text{K/W]} \quad (5)$$

$$R_{cond} = 4.17 \cdot 10^{-6} \text{ [m}^2\text{K/W]}$$

$$R_{conv,LH2} = 7.31 \cdot 10^{-5} \text{ [m}^2\text{K/W]}$$

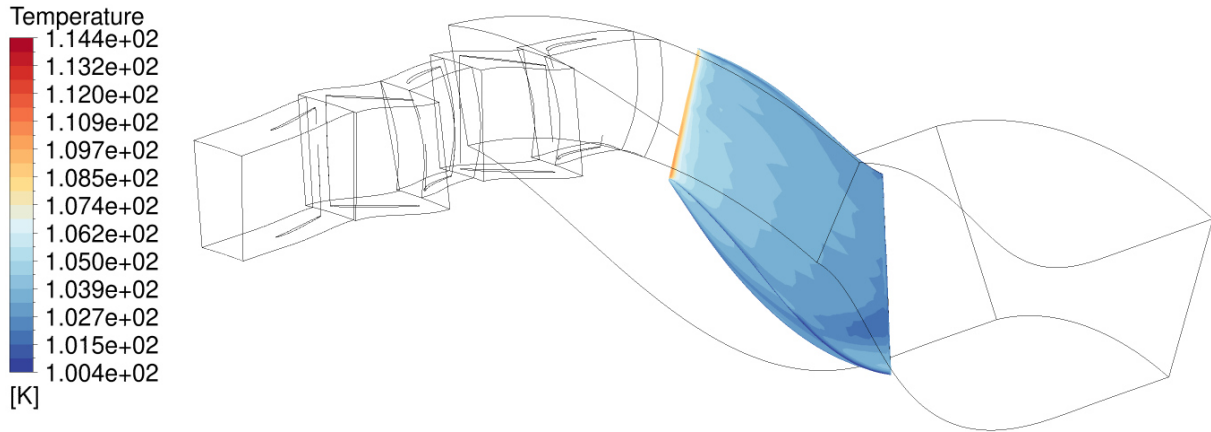


Figure 9 - Wall temperature for the ICD.

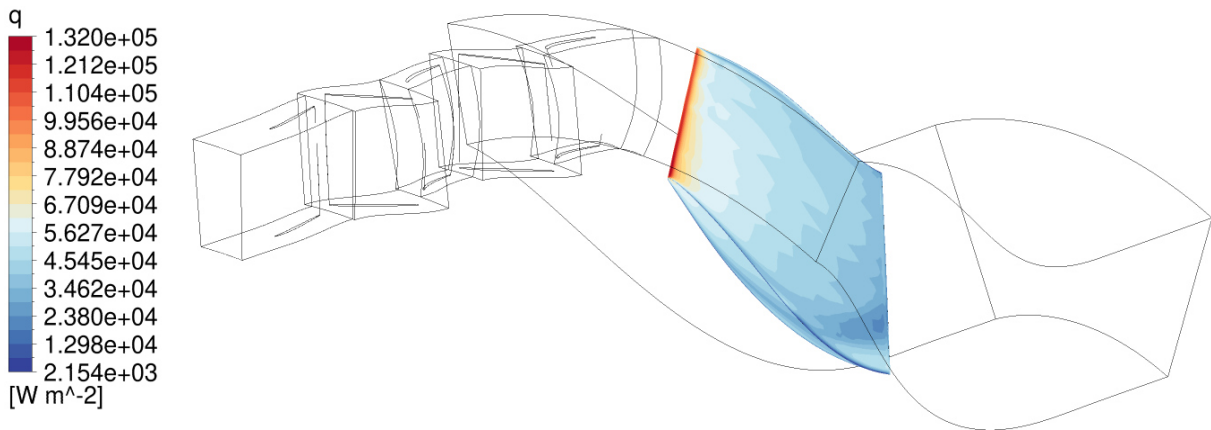


Figure 10 - Wall heat flux for the ICD.

4.1.4 Heat transfer on S2

The approach outlined in the previous section (4.1.3) regarding heat transfer boundary conditions has also been applied to Stator 2 (S2) since it has a large amount of surface area. The main difference here is that the bulk temperature for evaluating the heat transfer for LH2 flow in the cooling channels is iterated on since the hydrogen experiences a relatively large bulk temperature increase. The results below show that a much larger amount of heat transfer potential exists for S2 than for the ICD due to its larger surface area and higher average heat transfer coefficient. The overall heat flow was 59.69 kW ($\Delta T_0 = -3.37 \text{ K}$). S2 also features a lower pressure loss compared to the design point simulation. As for the ICD, the wall temperatures are extremely low (Figure 11).

$$\begin{aligned}
 p &= 42 \text{ bar} \\
 T_{LH2,mid} &= 110.6 \text{ K} \\
 \dot{m}_{LH2} &= 0.1840 \text{ kg/s} \\
 N_{channels_per_vane} &= 64 \\
 Re &= 9871.5 \\
 Nu &= 29.95 \\
 h_{conv,LH2} &= 5957 \text{ [W/m}^2\text{K]} \\
 U &= 5812 \text{ [W/m}^2\text{K]}
 \end{aligned}
 \tag{6}$$

Table 10 – Overall results for the cryogenic S2 simulation

S2 cooling	
Corrected mass flow [kg/s]	18.45
Q S2 vane [kW]	59.69
Equivalent core air temperature drop ΔT_0 [K]	3.37
Vane surface area [m ²]	1.033
Ave. heat transfer coeff. ICD vane [W/m ² K]	335.6

Table 11 - Total pressure losses for each stator for the cryogenic S2 simulation. The pressure losses have been normalized with the total pressure at the inlet of each respective stator domain.

	IGV	S1	S2	ICD
Total pressure loss:	0.063%	0.099%	0.123%	0.106%

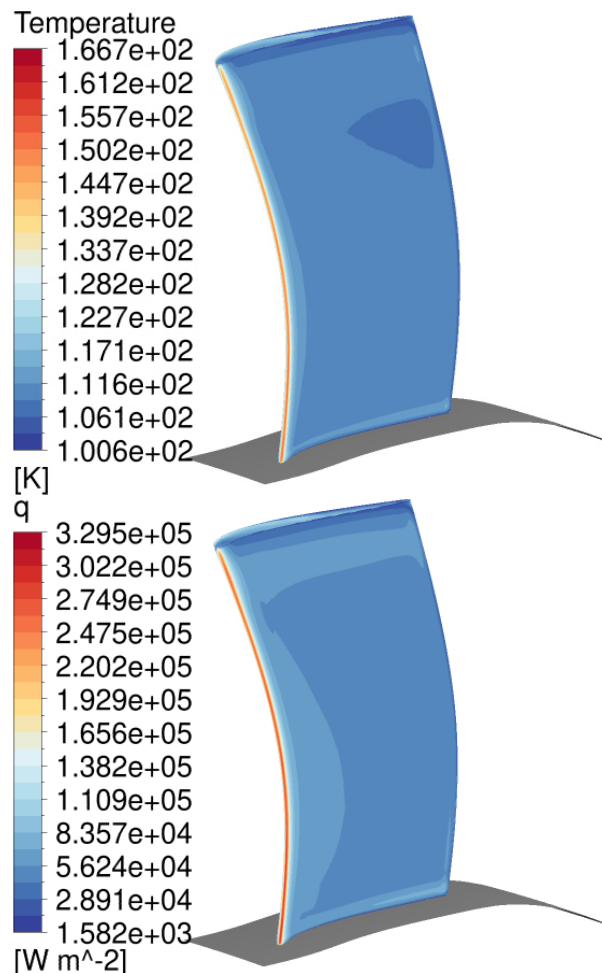


Figure 11 - **Top:** Wall temperature for the S2. **Bottom:** Wall heat flux for the S2.

4.1.5 Heat transfer on all stators

The aim here was to maximize the amount of heat transfer surface by applying the cooling to all stators (IGV, S1, S2, ICD) in the ENABLEH2 compressor. This was carried out in the same approach as in the previous sections but with the LH2 massflow divided between all four stators in order to reach similar values for the overall heat transfer coefficient U , resulting in 10% of the LH2 massflow for the ICD and the rest divided equally between the IGV, S1, and S2 stators. The details for each boundary condition are shown below in Table 12. The hydrogen temperature at midspan $T_{mid,LH2}$ has been iterated.

Table 12 – LH2 boundary conditions for all stators.

	IGV	S1	S2	ICD
p [bar]	42	42	42	42
$T_{mid,LH2}$ [K]	115.4	122.4	125.8	124.82
\dot{m}_{LH2} [kg/s]	0.0552	0.0552	0.0552	0.0184
$N_{channels_per_vane}$	64	64	64	318
Re	2888	2787	2740	2863
Nu	9.59	9.04	8.72	9.45
$h_{conv,LH2}$ [W/m ² K]	1996	2003	1988	2138
U [W/m ² K]	1980	1986	1971	2119

The overall results for this simulation are shown in Table 13. It can be seen that the achieved overall heat flow for all stators amounts to 129 kW or an equivalent 7.31 K core air temperature drop. The largest share of the heat flow is through the S2 stator while the ICD stator provides the smallest amount of heat flow. The obtained wall temperatures range from approximately 120 K in the coldest parts of the surface to 225 K in the leading edge of the S2 stator.

Table 13 – Overall results for the case with cooling on all stators

Cooling all stators	
Corrected mass flow [kg/s]	18.71
Overall Q [kW]	129.1
Equivalent core air temperature drop ΔT_0 [K]	7.31
IGV	
Q [kW]	26.62
Surface area [m ²]	0.635
Ave. heat transfer coeff. [W/m ² K]	282.5
S1	
Q [kW]	40.09
Surface area [m ²]	0.878
Ave. heat transfer coeff. [W/m ² K]	325.0
S2	
Q [kW]	47.31
Surface area [m ²]	1.033
Ave. heat transfer coeff. [W/m ² K]	332.0
ICD	
Q [kW]	15.03
Surface area [m ²]	0.448
Ave. heat transfer coeff. [W/m ² K]	228.9

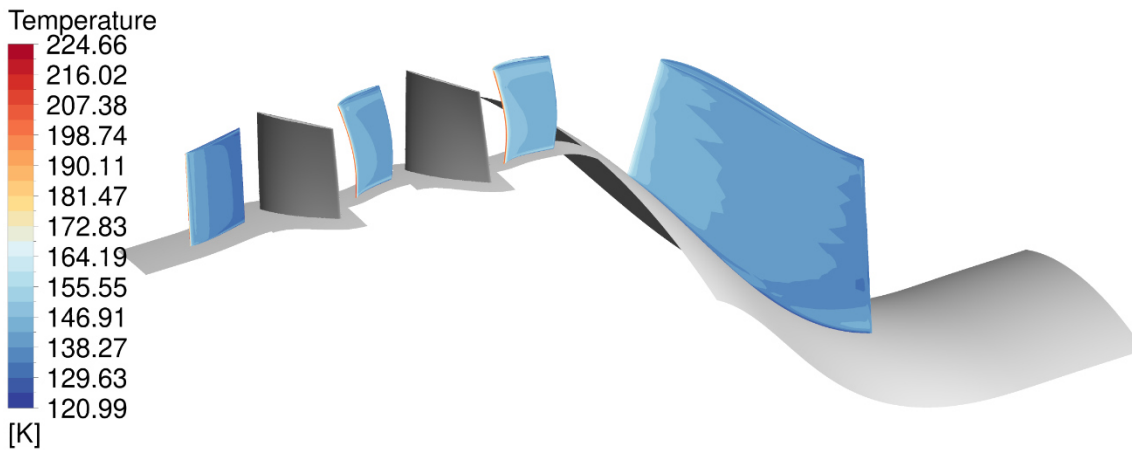


Figure 12 -**Top**: Wall temperature for all cooled stators. **Bottom**: Wall heat flux all cooled stators. Note that the negative values for heat flux are due to the direction convention used by CFX for its surface normal vectors.

4.1.6 Conjugated ICD simulations

A conjugated CFD simulation has been carried out for a simplified cooling channel geometry to assess the viability of the BC methodology used in the previous sections. The case was set up as follows:

- The vane is modelled as a solid with the same thermal conductivity of 120 [W/m K] (same as used in sections 4.1.3 to 4.1.5). The specific heat of the solid material is set as 903 [J/kg K].
- Six cooling channels with square cross-sections (4x4 mm) are incorporated inside the vane where the LH2 flows. The hydrogen massflow of 0.1840 [kg/s] is divided equally between each ICD and each cooling channel.
- The hydrogen temperature and pressure at the inlet are 100 K and 42 bar, respectively.
- The LH2 is modelled as a real fluid with thermophysical data from REFPROP [18].

The overall heat flows for this conjugated case and the ICD case from section 4.1.3 are shown in Table 14 where it can be seen that the overall heat flow Q for the ICD vanes in the conjugated CFD case is approximately 20% lower than for the ICD case from 1. This is due to the fact that the cooling channel geometries are quite different, especially considering the thickness of the solid material between the LH2 cooling channels and the core air flow compared to what was assumed in section 4.1.3. This has resulted in somewhat different wall temperatures for the vane when comparing the conjugated case with original ICD case, as shown in Figure 13, resulting in the largest difference in temperatures near the leading and trailing edges, due to the large distance from to closest cooling channel. On the other hand, there is good agreement for the heat transfer coefficients on the air side of the vane, as is evidenced by Figure 14.

The cooling channel geometry used for the conjugated simulation is somewhat simplified; a more mature design should feature more numerous cooling channels located closer to the vane surface, effectively approaching the setup for the BC methodology used in this report and increasing overall heat flow Q .

Table 14 – Overall results for the ICD simulations.

	ICD	ICD conjugated
Q ICD vane [kW]	20.53	16.01
Equivalent core air temperature drop ΔT_0 [K]	1.18	0.92
Ave. heat transfer coeff. ICD vane [W/m ² K]	240.1	218.3

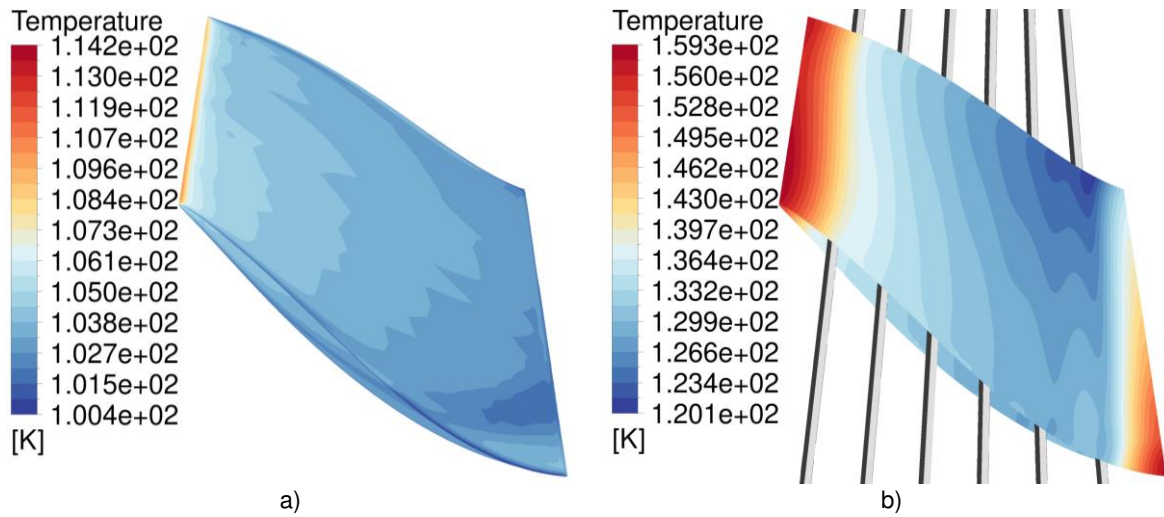


Figure 13 – Wall temperatures for the a) ICD simulation from section 1 and b) for the conjugated case.

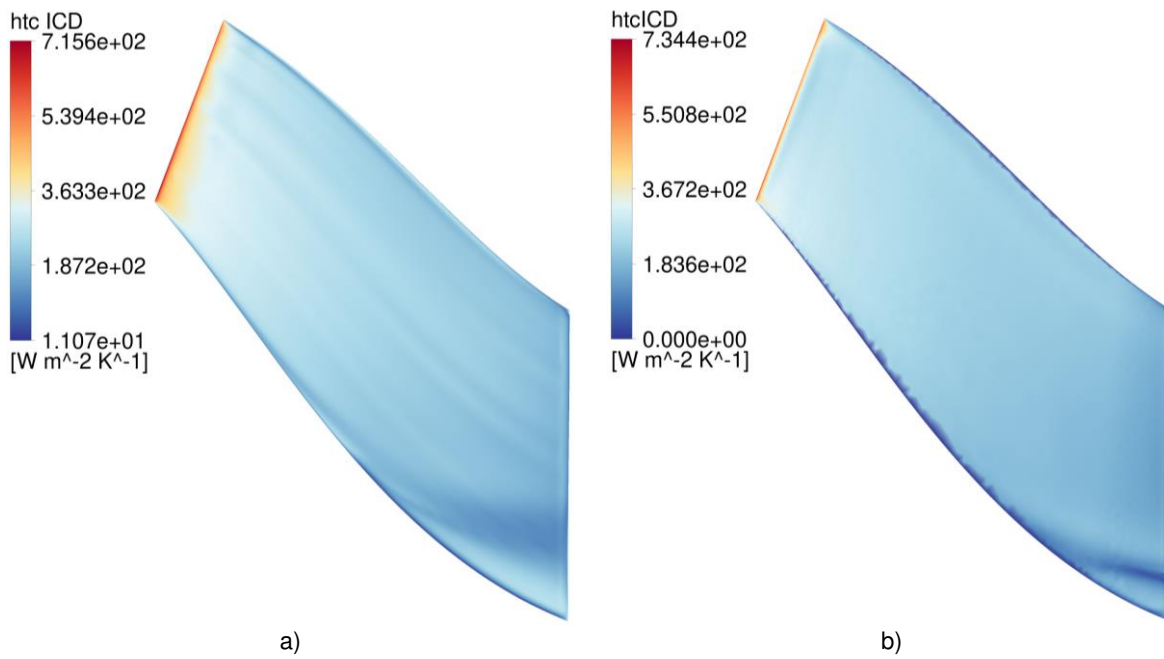


Figure 14 – Convective heat transfer coefficients for the a) ICD simulation from section 1 and b) for the conjugated case.

4.1.7 Effect of transition on cryogenic cooling

Laminar-turbulent transition can influence the local heat transfer coefficient on the stator surfaces. Therefore, this section of the report will investigate the impact on heat transfer by incorporating the Gamma-Theta transition model into the CFD model used in section 4.1.5. As in previous cases, the hydrogen temperature at midspan $T_{mid,LH2}$ has been iterated on and the final LH2 boundary conditions are as shown in Table 15.

Table 15 – LH2 boundary conditions for all stators for the transition case. Pressures and massflows are as in Table 12.

	IGV	S1	S2	ICD
$T_{mid,LH2}$ [K]	108.8	116.1	120.3	121.415
Re	2990	2876	2817	2912
Nu	10.1	9.53	9.22	9.69
$h_{conv,LH2}$ [W/m ² K]	1964	1999	2005	2129
U [W/m ² K]	1948	1982	1989	2110

Table 16 – Overall results for the case with cooling on all stators, with and without transition.

Cooling all stators including transition	Without transition	With transition
Corrected mass flow [kg/s]	18.71	19.08
Overall Q [kW]	129.1	92.7
Equivalent core air temperature drop ΔT_0 [K]	7.31	5.15
IGV		
Q [kW]	26.62	15.17
Ave. heat transfer coeff. [W/m ² K]	282.5	152.0
S1		
Q [kW]	40.09	28.62
Ave. heat transfer coeff. [W/m ² K]	325.0	218.7
S2		
Q [kW]	47.31	36.30
Ave. heat transfer coeff. [W/m ² K]	332.0	239.27
ICD		
Q [kW]	15.03	12.61
Ave. heat transfer coeff. [W/m ² K]	228.9	183.6

Overall heat flow has dropped to 92.7 kW, and the IGV has suffered the largest proportional drop in heat flow since the flow has become mostly laminar when including transition in the CFD model, as is visible in Figure 15. This figure together with Figure 16 shows that at midspan the flow is laminar for the IGV and the S1 and S2 pressure sides, while the suction sides of the S1 and S2 stators undergo transition close to the mid-chord position. For the ICD the flow undergoes transition on both the pressure and suction side at a similar location, as evidenced by the sudden increase in heat transfer coefficient when the flow becomes turbulent. This behavior is representative for most parts of the IGV, S1, and S2 stators along the span direction, as is visible in Figure 17 and Figure 18, while the ICD features more variation with respect to the location of transition.

While the impact of transition on the heat flow for the ENABLEH2 compressor is relatively large it will be less impactful for a high-speed LPC geometry such as VINK due to its higher Reynolds number (see Figure 7), which will result in earlier onset to turbulence and larger portions of the stator surfaces in fully turbulent flow.

Cooled surfaces are known to delay transition. This was investigated in a previous paper by the authors [26] which found that colder wall temperatures on the ICD vane led to the transition moving further downstream, even though this change was relatively small and only led to the transition moving downstream by approximately 1% chord for a decrease in wall temperature of 80 K.

4.1.8 Conclusions on intercooling using existing aero surfaces

- A relatively low amount of heat transfer can be achieved on existing aero surfaces. The calculations in this section have shown that for the ENABLEH2 compressor geometry the largest heat flow obtained was 129.1 kW when utilizing all stator surfaces, which corresponds to a core air temperature decrease of approximately 7 K (+44 K for the LH2).
- Only the stator surfaces have been used for heat transfer. There is additional surface area in the hub and shroud of the stators which could also be used for heat transfer.
- The effect of transition was seen to decrease the amount of heat transfer obtained compared to a fully turbulent case due to large areas of laminar flow.
- The ENABLEH2 compressor constitutes a low-speed design for implementation in a test rig. A high-speed design such as VINK should feature higher Reynolds numbers, earlier onset to turbulence, larger portions of the stator surfaces in fully turbulent flow, and therefore higher amounts of heat transfer.

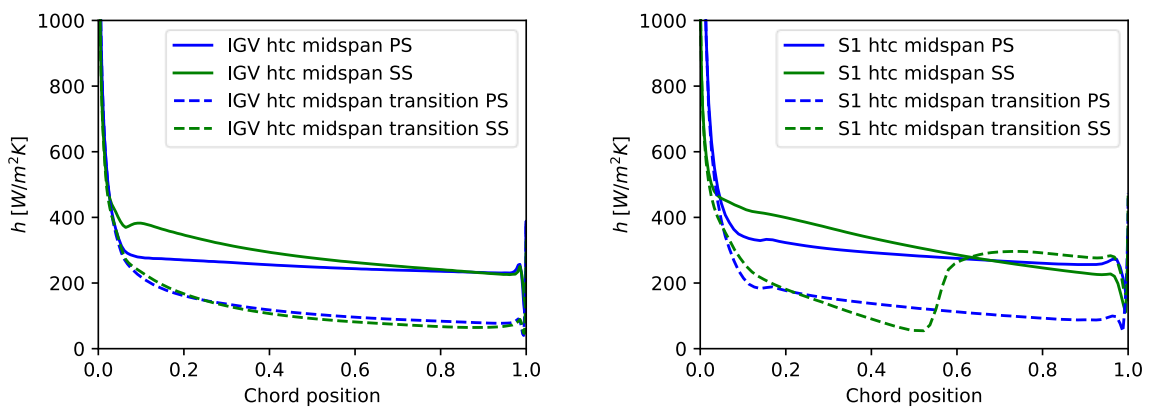


Figure 15 – Heat transfer coefficient h at midspan for the IGV (left) and S1 (right) with and without transition modelling.

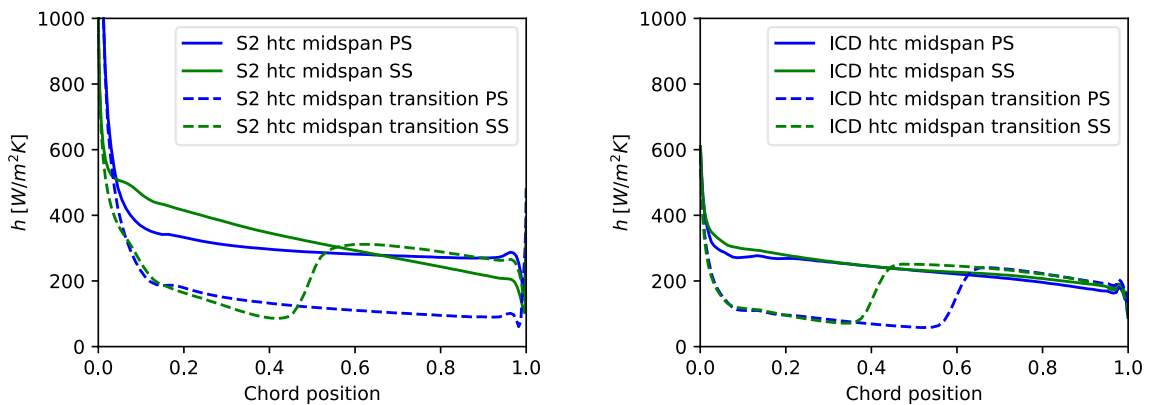


Figure 16 - Heat transfer coefficient h at midspan for the S2 (left) and ICD (right) with and without transition modelling.

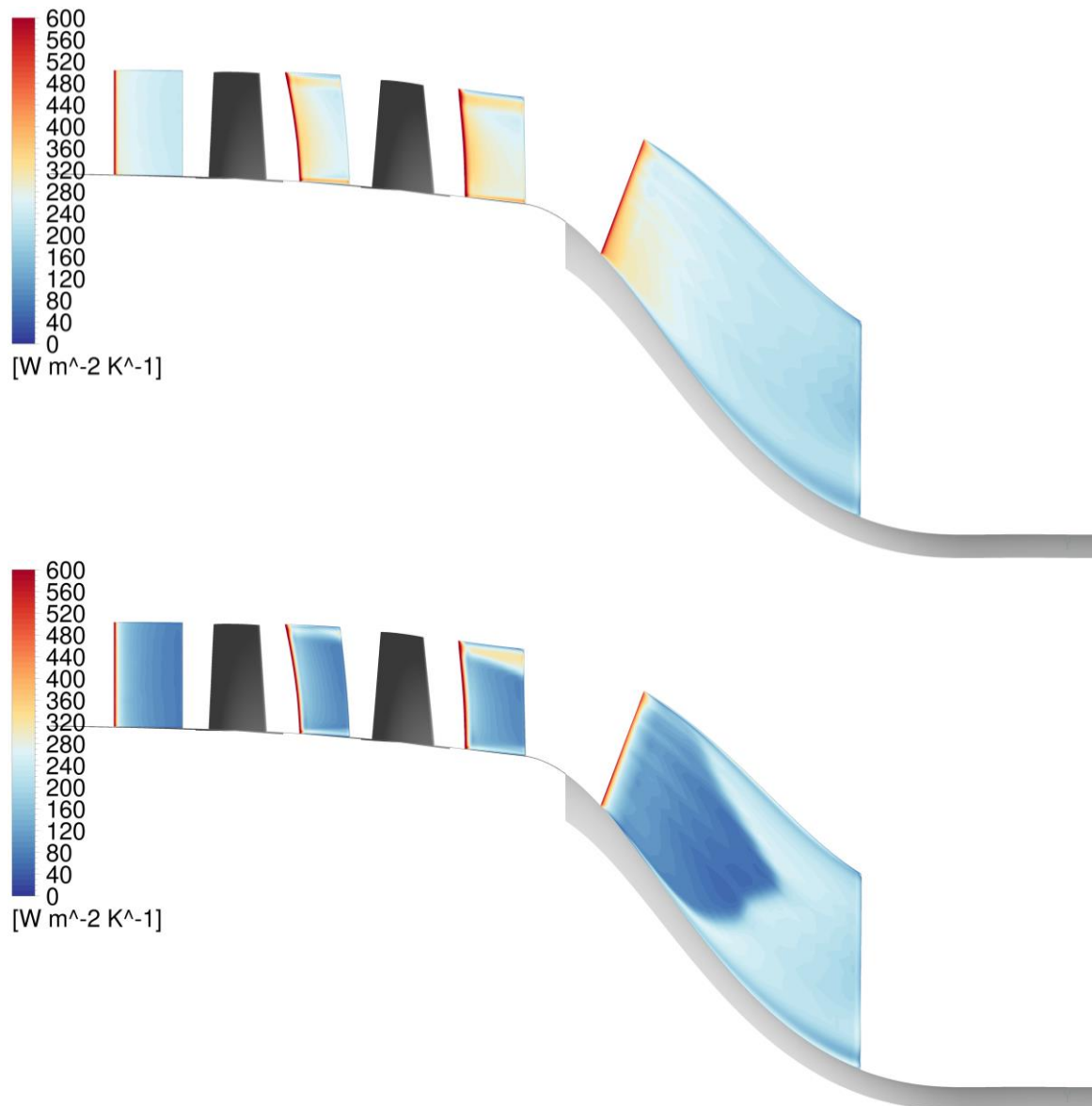


Figure 17 – Convective heat transfer coefficient h for the pressure sides of the IGV, S1, S2, and ICD stators for the case without transition (upper) and with transition (lower). The upper range of the color scale has been capped at 600 $[W/m^2K]$ for improved readability.

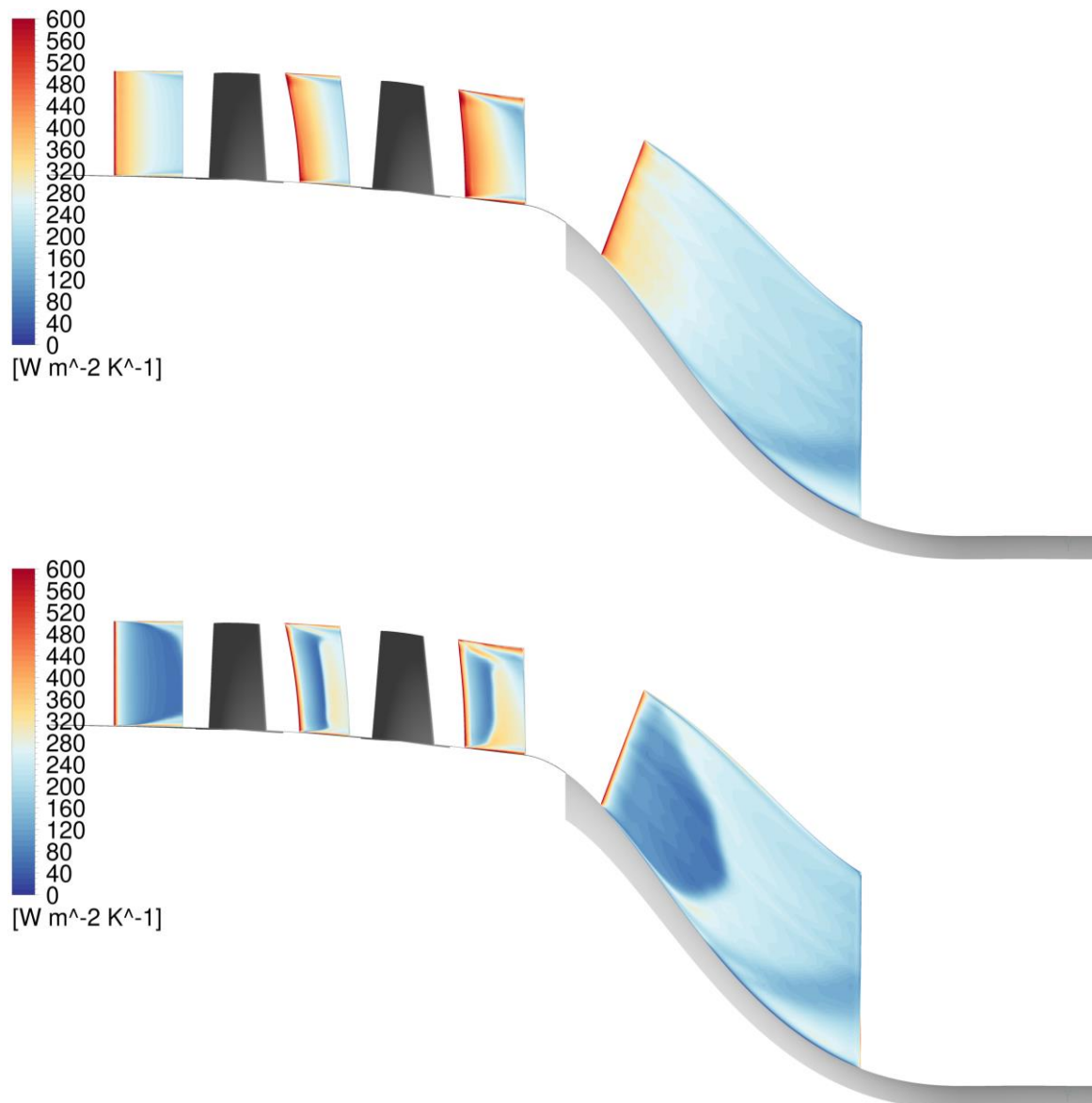


Figure 18 – Convective heat transfer coefficient h for the suction sides of the IGV, S1, S2, and ICD stators for the case without transition (upper) and with transition (lower). The upper range of the color scale has been capped at 600 $[W/m^2K]$ for improved readability.

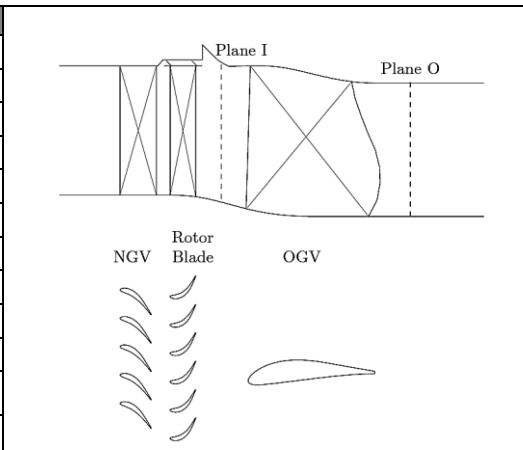
4.2 Recuperation

For the present report, recuperation refers to using core exhaust air (extracted after the low-pressure turbine) to pre-heat the hydrogen fuel prior to combustion. Hence, recuperation is primarily used to increase the fuel enthalpy. The present section evaluates the aerothermal performance of existing turbomachinery surfaces for heat transfer at the engine exhaust.

In the present section the aerothermal performance of conventional turbomachinery surfaces is numerically evaluated using previously validated RANS models. More information about validation and experimental data is provided in deliverable 2.3. Two configurations with equal solidity and varying aspect ratio are investigated with respect to heat-transfer performance in cold-flow low-speed conditions (like those found in Chalmers low-pressure turbine outlet guide vane facility). The relevant geometric parameters and design point operating conditions are listed in Table 17 together with a meridional cut of the test section.

Table 17 – Geometrical characteristics and design point performance parameters at Chalmers low-pressure turbine outlet guide vane facility.

Design conditions	Baseline	Splitter	Main
Corr. mass flow (kg/s)	23.55	12	12
Axial Velocity (m/s)	31.7	16	16
Reynolds (height based)	465,000	235,000	235,000
Avg. Tip radius (m)	0.553	0.553	0.553
Avg. Hub radius (m)	0.34	0.34	0.34
Inlet HTR	0.614	0.614	0.614
Outlet HTR	0.582	0.601	0.601
Flow coefficient (Turbine)	0.622	0.622	0.622
Stage loading (Turbine)	1.153	1.153	1.153
Mid-span chord (m)	0.2164	0.0734	0.120
Number of Vanes	12	12	12
Avg Aspect Ratio	1.14	3.64	2.3



Structured, hexahedral meshes for the different computational domains are again generated using ANSYS Turbogrid, see Figure 19. Enough resolution close to the walls is ensured to properly resolve the thermal and flow boundary layers, the first node height of the mesh in the near wall region was set

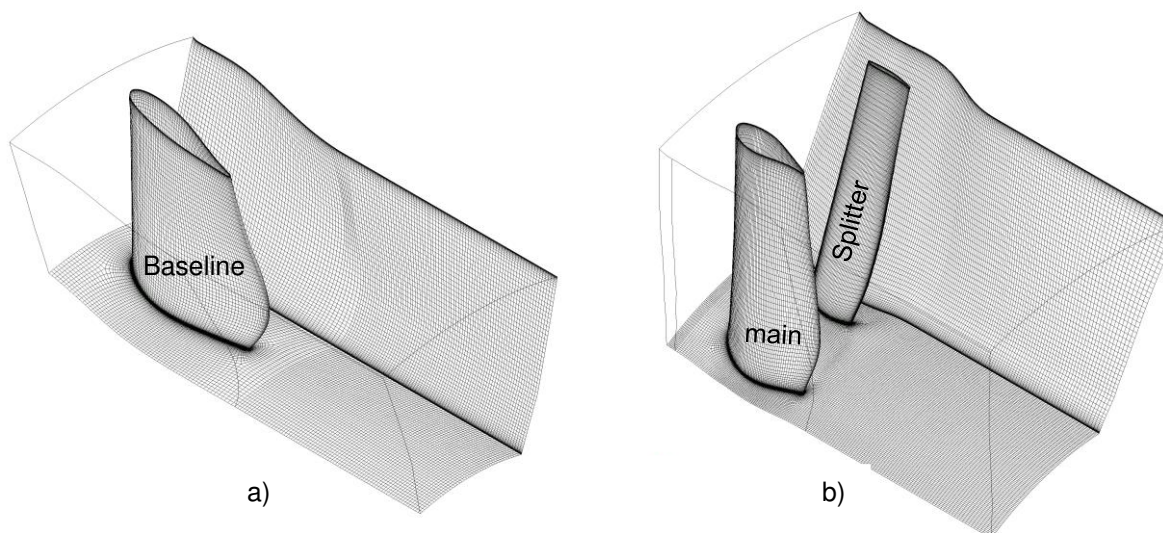


Figure 19 – Numerical domains used to simulate the aerothermal performance of the baseline (a) and high-aspect ratio (b) TRS geometries. The high-aspect-ratio configurations includes two separate and different vanes (main and splitter).

below $y^+ = 1$. ANSYS Fluent was used to simulate the flowfield, by solving the compressible flow Reynolds Averaged Navier-Stokes (RANS) equations together with the $k - \omega$ SST turbulence model

and the Gamma-Theta transition model. The working fluid is set as air semi-perfect gas with temperature dependent thermal conductivity and viscosity.

Regarding boundary conditions, at the inlet total pressure, total temperature and flow direction profiles extracted from the experimental data are imposed at the domain boundary. Turbulent intensity and length scale are defined to match the measured turbulence decay across the test section. At the outlet, a static pressure profile is varied to match the desired mass flow. At the wall, a non-slip boundary condition is imposed together with a constant wall temperature.

4.2.1 Heat transfer on the baseline TRS vane

The chosen approach for modelling the heat transfer consists of imposing a fixed wall temperature to be able to establish the heat-transfer coefficient on the external side of the vane. As shown in the ICD calculations, above, the overall heat transfer coefficient is dominated by the performance on the air side. Hence, fixing the wall temperature should provide reasonably good estimates of the overall heat transfer capability of the TRS surfaces without the need of assessing the internal performance of the hydrogen cooling channels. The simulated conditions, listed in Table 18, replicate the cold flow experimental results at turbine half-speed conditions ($Re = 235,000$). Furthermore, the simulations are carried out with the SST transition turbulence model, and therefore account for the contribution of the laminar flow boundary layer to the average heat-transfer coefficient.

Table 18 –Computed flow conditions for the baseline TRS test case.

	Inlet	Outlet
p (Pa)	99952	99928
p_0 (Pa)	100117	100109
C (m/s)	16.3	16.9
Flow Angle (deg)	-13.9	0.80
Mass flow (kg/s)	11.8	11.8

The results computed for the heat-transfer coefficient (htc) on the baseline TRS vane are shown in Figure 20 and Figure 21. Figure 20 shows the contour plots of htc in the suction side of the vane and Figure 21 shows the variation of htc with the normalized chord at three different span locations. The transition from laminar to turbulent is observed at about 40-50% of the chord length at about mid-span, visible in Figure 21-b). Also, as expected one can easily identify that the stagnation region, in the leading edge, provides the maximum heat flux.

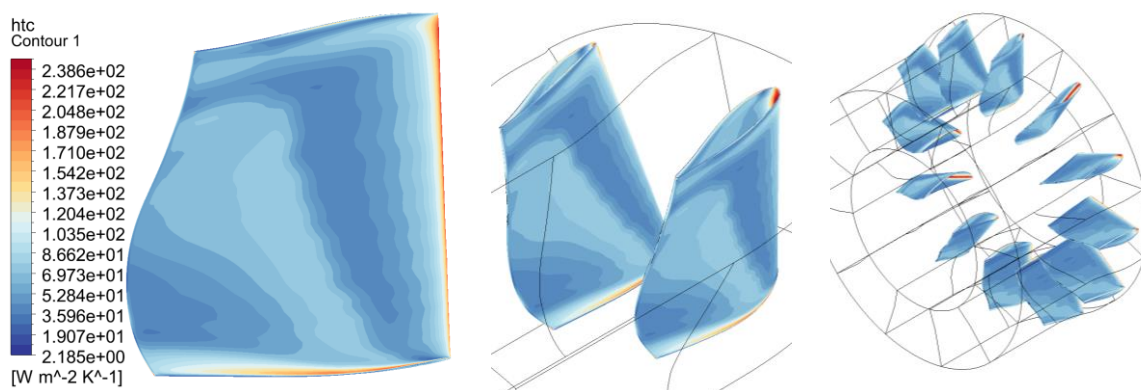


Figure 20 – Heat transfer coefficient contour plots computed for the baseline TRS.

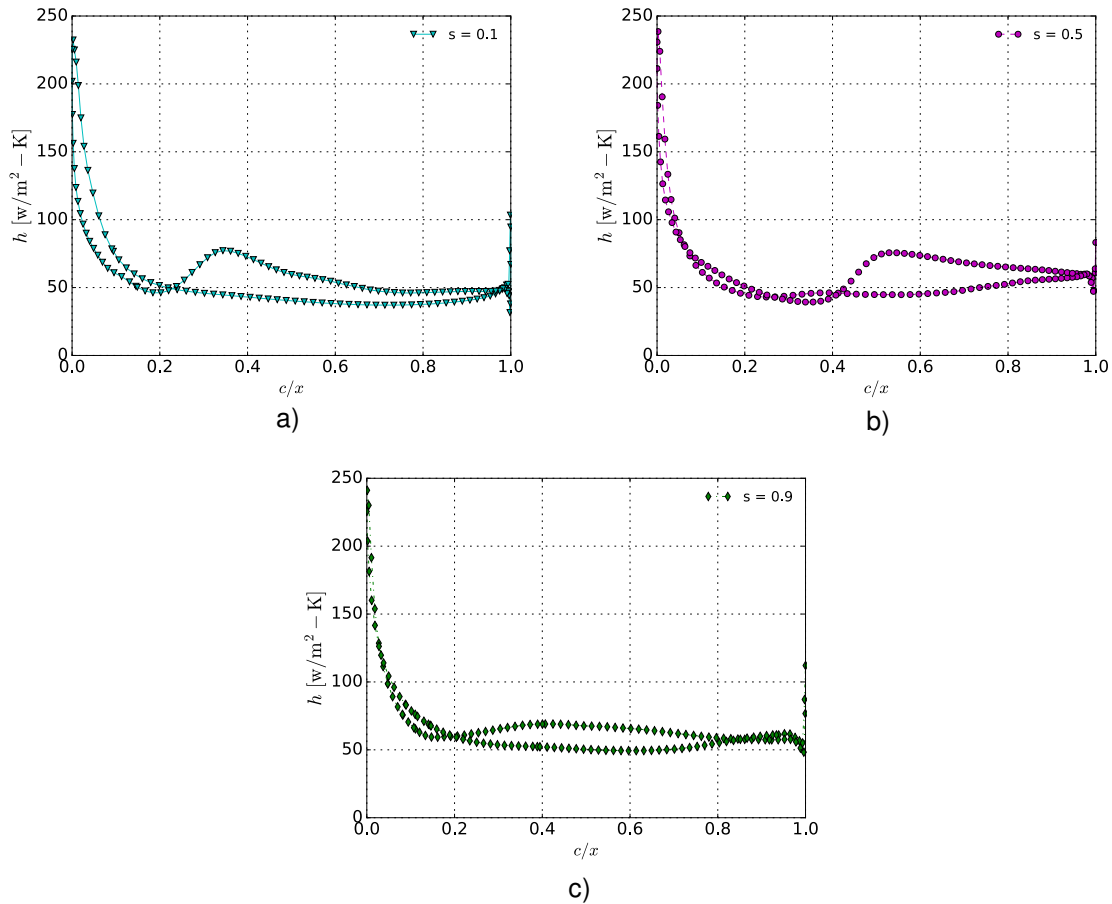


Figure 21 – Variation of heat-transfer coefficient along the normalized vane chord for different span fractions: a) 10% span; b) 50% span; c) 90% span.

4.2.2 Heat transfer on the high-aspect ratio TRS

For the same wetted area, high-aspect ratio vanes are expected to maximize average heat transfer. Hence, a designer looking into maximizing heat transfer on the TRS would try, for a constant solidity, to progressively increase the number of vanes, until mechanical and aerodynamic constraints come into play. In the current report this effect was modeled by adding a splitter vane in between each main vane and also by reducing the chord of both vanes in an attempt to keep solidity unchanged in relation to the baseline case. The chosen approach for modelling the heat transfer in the high-aspect ratio TRS follows the same approach as the conventional one. The simulated conditions, listed in Table 19, replicate the cold flow experimental results at turbine half-speed conditions ($Re = 235,000$). Again, the simulations are carried out with the SST transition turbulence model, and therefore account for the contribution of the laminar flow boundary layer to the average heat-transfer coefficient.

Table 19 – Computed flow conditions for the high-aspect ratio TRS test case.

	Inlet	Outlet
p (Pa)	101422	101384
p_0 (Pa)	101585	101577
C (m/s)	16.1	17.5
Flow Angle (deg)	-15.9	0.7
Mass flow (kg/s)	11.9	11.9

The isolines of constant heat-transfer coefficient (htc) on the high aspect ratio TRS vane (main and splitter) are shown in Figure 22. Figure 23 shows the variation of htc with the normalized chord at three different span locations and the contribution of the separate vanes. When compared to the baseline TRS, due to the lower chord based Re number, transition is observed to take place later across the different computed spans. However, the average htc is expected to be much higher due to an increase in blade count and associated increase in regions of maximum heat-flux (stagnation).

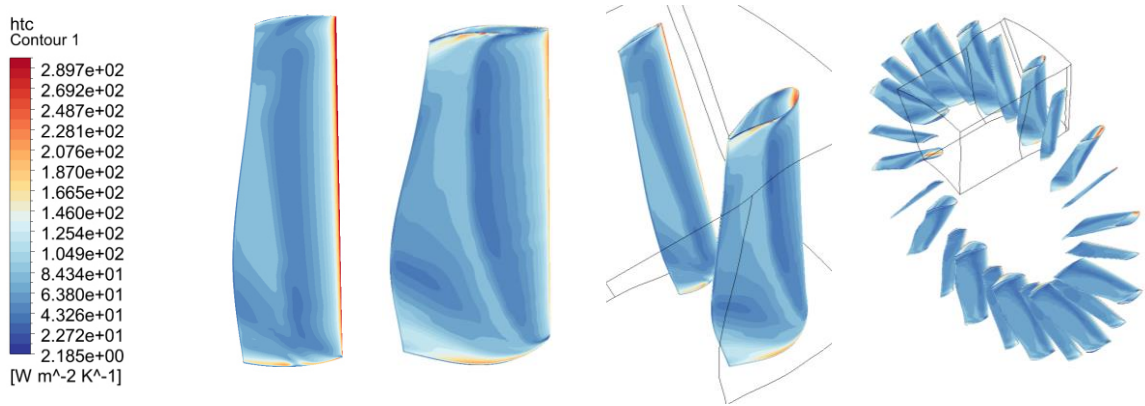


Figure 22 – Heat transfer coefficient contour plots computed for the high aspect ratio TRS.

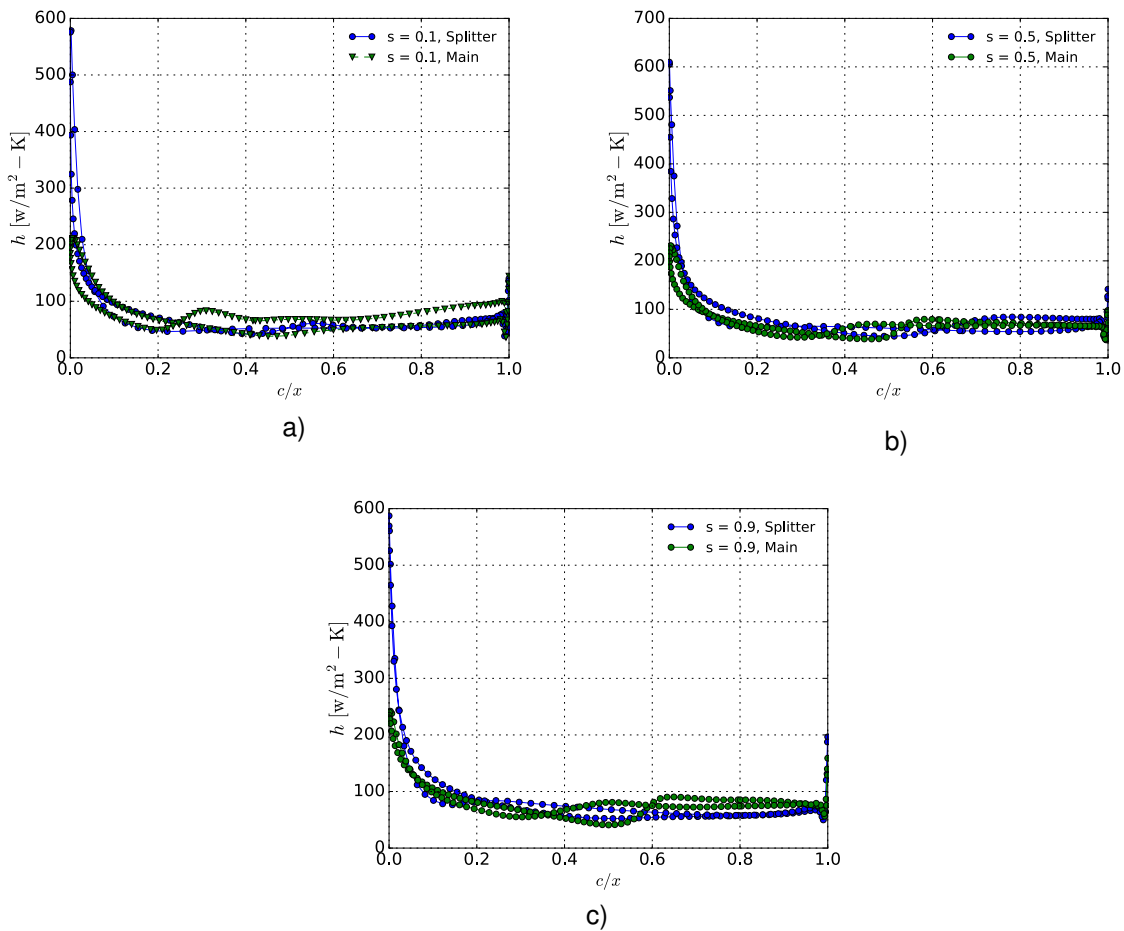


Figure 23 – Variation of heat-transfer coefficient along the normalized vane chord for different span fractions in the high-aspect ratio TRS: a) 10% span; b) 50% span; c) 90% span.

4.2.3 Heat transfer on fully turbulent high-aspect ratio TRS

The last test case comprises the simulation of a fully turbulent flow on the high aspect-ratio TRS. As shown in the previous section, the extension of laminar flow across the blades is substantial which hinders the heat-transfer potential. One possible action is to trigger turbulence at the vane leading edge and increase the heat transfer coefficient while accepting a slight increase in pressure loss. The chosen approach for modelling the heat transfer follows the previous test cases and the simulated conditions, are listed in Table 20. These again replicate the cold flow experimental results at turbine half-speed conditions ($Re = 235,000$). This time, the simulations are carried out with the k- ω SST turbulence model, and therefore assume a fully developed turbulent flow at the domain inlet.

Table 20 – Computed flow conditions for the high-aspect ratio TRS test case.

	Inlet	Outlet
p (Pa)	101422	101382
p_0 (Pa)	101585	101576
C (m/s)	16.1	17.5
Flow Angle (deg)	-15.9	0.32
Mass flow (kg/s)	11.9	11.9

The isolines of constant heat-transfer coefficient (htc) on the fully turbulent high aspect ratio TRS vane (main and splitter) are shown in Figure 24. On the other hand, Figure 25 shows the variation of htc with the normalized chord at three different span locations and the contribution of the separate vanes. When compared to the previous high-aspect ratio TRS, one can observe a slight increase in htc along the different span locations.

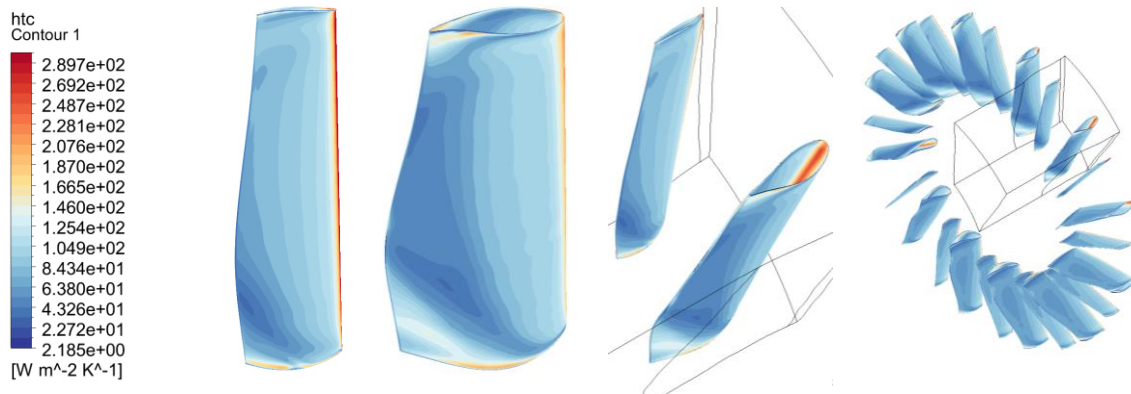


Figure 24 – Heat transfer coefficient contour plots computed for the fully-turbulent high aspect ratio TRS. Value is capped at $300 \text{ W/m}^2\text{-K}$ to improve visibility.

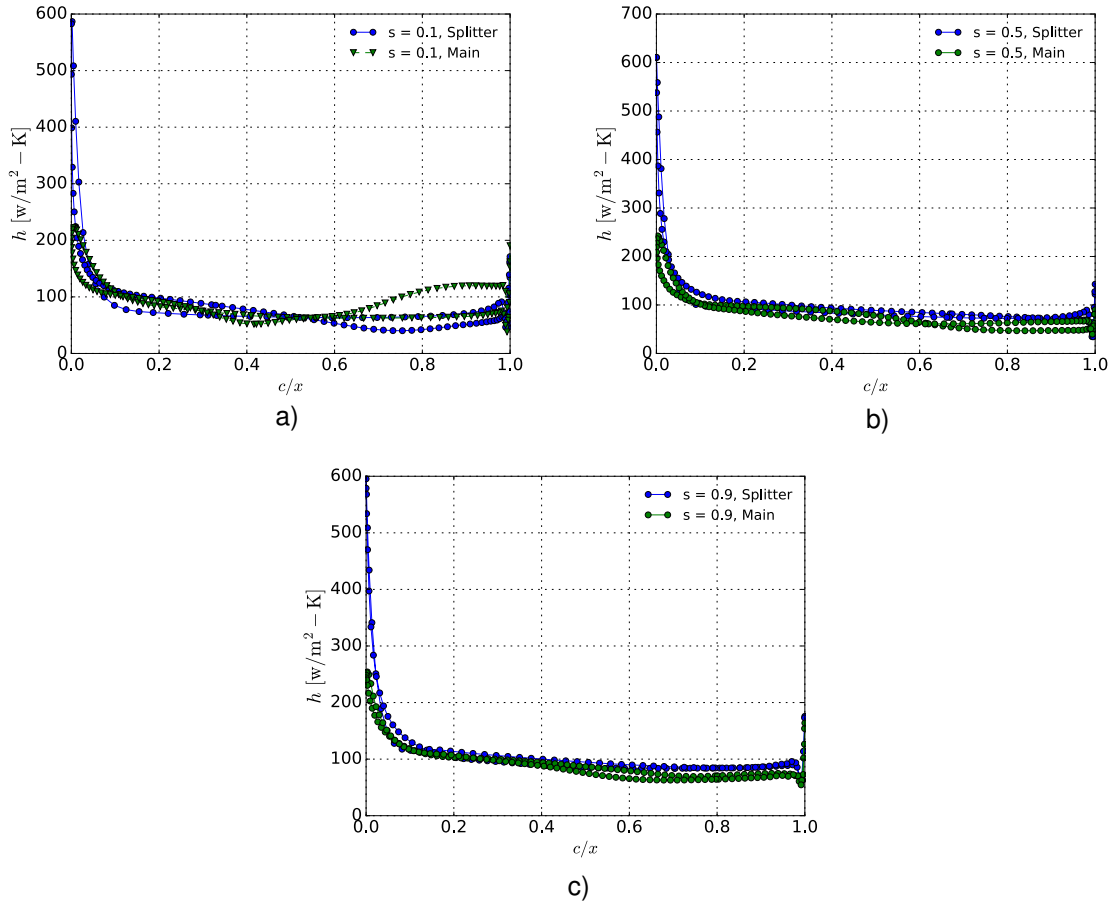


Figure 25 – Variation of heat-transfer coefficient along the normalized vane chord for different span fractions in the fully turbulent high-aspect ratio TRS: a) 10% span; b) 50% span; c) 90% span.

4.2.4 Comparison between the different TRS geometries and heat transfer potential for LH2

The comparison between the aerothermal performance of the different TRS geometries is listed in Table 21. One can observe that increasing the average aspect ratio by a factor of 2.6 leads to equivalent increase in average heat-transfer coefficient, with a 1.6% increase in total pressure losses. Triggering turbulence leads to further increase in htc but at a higher cost of pressure loss, approximately 16% increase in htc, relative to the high aspect ratio TRS, leads to 16% increase in total pressure loss.

Table 21 – Overall results for the Baseline TRS simulation.

	TRS baseline	TRS high aspect-ratio	TRS turbulence triggering
Vane surface area [m ²]	1.18	1.243	1.243
Ave. heat transfer coeff (HTC) [W/m ² K]	63	155	180.4
ξ (total pressure loss coefficient)	0.0485	0.0493	0.0570
$\Delta\xi$ to baseline	Datum	+1.6%	+17.5%
ΔHTC to baseline	Datum	+146%	+185%

The total pressure loss coefficient is calculated using,

$$\xi = \frac{(p_{0,in} - p_{0,out})}{p_{dyn,in}} \quad (7)$$

Nevertheless, looking into the heat transfer potential for LH2. Table 22 shows the achievable temperature variations in the engine core and fuel circuit for an external side air temperature of 294 K and assuming that LH2 could lead to an external wall temperature of 110 K. Moreover, it is assumed that the hydrogen mass flow is representative of the SMR engine above, i.e. for an air-fuel ratio of approximately 100.

Table 22 - The heat transfer potential for LH2.

	TRS baseline	TRS high aspect-ratio	TRS turbulence triggering
Vane surface area [m ²]	1.18	1.243	1.243
Ave. heat transfer coeff (HTC) [W/m ² K]	63	155	180.4
htc*Area [W/K]	74.3	192	224
Q [kW], for T _{wall} = 110K	13.7	35.3	41.3
Equivalent core air temperature drop ΔT_0 [K]	0.85 K	2.2 K	2.56 K
Equivalent H2 temperature increase ΔT_{H2} [K]	6.8 K	17.9 K	20.8 K

The results obtained are aligned with what was observed in the ICD calculations above, i.e. existing surfaces provide very limited heat exchanger area and only provide marginal changes into the core flow and H2 temperatures. Increased exhaust temperature and speed for more realistic cases will allow for increased temperature variations, but still substantially below the ranges offered by compact heat-exchanger technology, which will be addressed in the next section.

4.3 Compact heat exchanger design and integration

This section provides a walkthrough of the design methodology employed to design and integrate a compact heat exchanger into the core air stream of the baseline engine from section 3.1. The methodology is first applied on a compact heat exchanger in the interconnecting compressor duct (ICD) but its methods and results will also be applicable for recuperation.

4.3.1 Compact heat exchangers

In order to accommodate larger amounts of heat transfer more surface area is required, which will come at a cost of increased pressure losses. One approach for overcoming this is to first diffuse the flow in order to decrease the dynamic pressure and then use a compact heat exchanger due to their large surface-to-volume ratios and relatively low pressure losses.

An example of a design of a heat exchanger integrated into an ICD duct compatible with the LPC outlet and HPC inlet in Figure 5 is shown in Figure 26. The flow goes from left to right and starts at a straight annular channel corresponding to the inner and outer radii of the LPC outlet. It is followed by a diffuser duct, a conical heat exchanger (HEX), and then a contraction which connects to the downstream HPC. The diffuser duct allows the flow to reach a specific inlet Mach number for the heat exchanger and is dependent on the area ratio between the inlet and outlet areas of the diffuser duct, as is shown Table 23.

Table 23 – Diffuser outlet Mach number for a series of area ratios. The area ratio is defined as the ratio between diffuser outlet and inlet areas. The inlet Mach number of the diffuser is 0.4.

Diffuser inlet Mach	Diffuser outlet Mach	Area ratio (AR)
0.400	0.400	1
	0.186	2
	0.091	4
	0.061	6
	0.046	8
	0.036	10

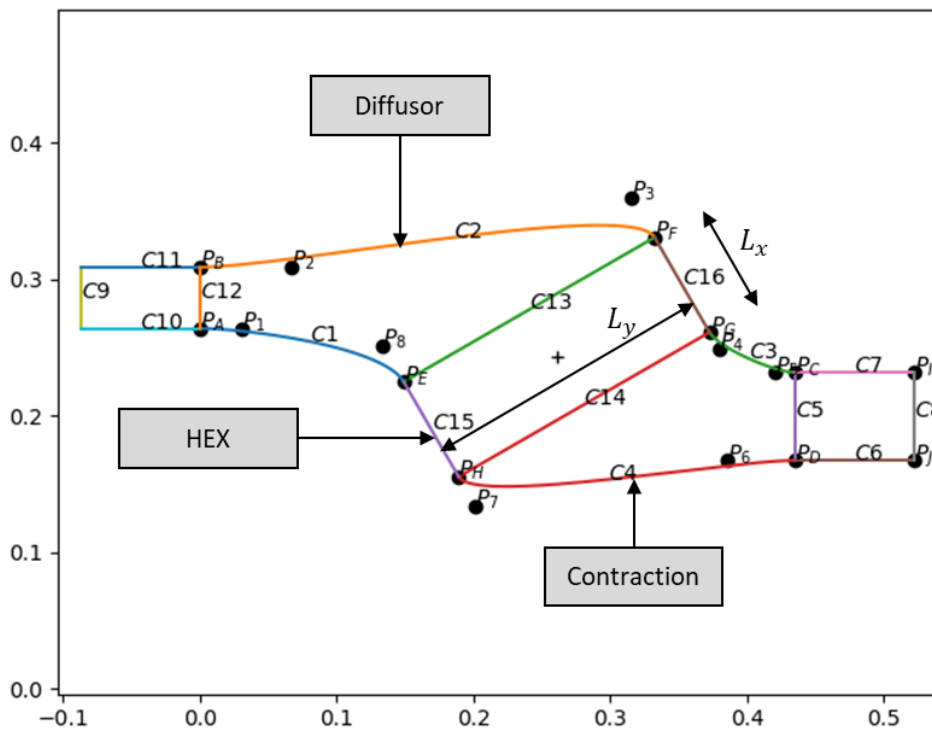


Figure 26 – Meridional view of a heat exchanger (bounded by curves C13 to C16) integrated into the ICD duct. The + sign in the HEX denotes the centroid of the cross-sectional area of the heat exchanger. L_x denotes the length of the HEX in the air direction while L_y is the length in the hydrogen flow direction. The circumferential length L_z is normal to this page and intersects the centroid (+) of the HEX.

Ref. [14] provides extensive amounts of data in terms of pressure drop and heat transfer correlations for a variety of compact heat exchanger configurations which can be used for conceptual design. These data is presented in terms of the Colburn j -factor ($j = StPr^{2/3}$) and friction factor f , as shown in Figure 27. The type of heat exchanger geometry chosen for this report is of the finned flat tube type with the designation 9.1-0.737-S whose geometry is illustrated in Figure 28.

The method for calculating the heat exchanger performance will be outlined in the next section.

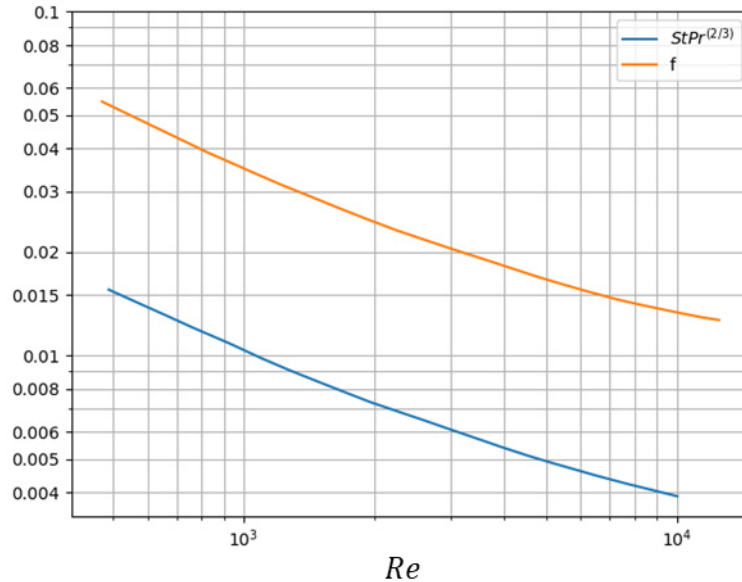


Figure 27 - Colburn j -factor ($j = StPr^{2/3}$) and friction factor f as function of Reynolds number for the 9.1-0.737-S finned flat tube heat exchanger.

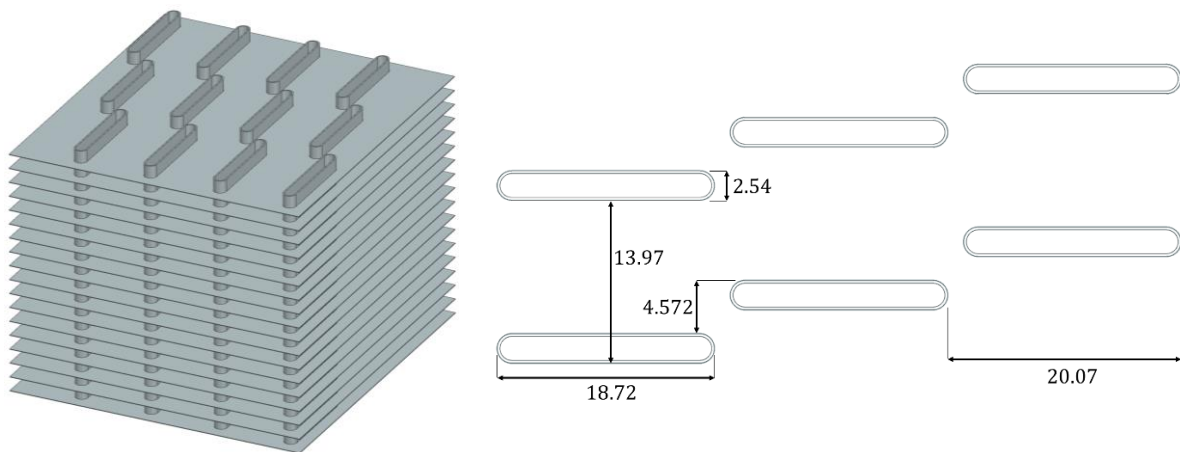


Figure 28 - Geometry of the 9.1-0.737-S finned flat tube heat exchanger. The schematic to the right is in [mm].

Table 24 –Heat exchanger 9.1-0.737-S properties.

Free-flow area/frontal area σ_{air}	0.788
Fin area/total area κ_{fin}	0.813
Fin spacing [mm]	2.794
Total air-side transfer area/total volume $\alpha_{air} [m^2/m^3]$	734.9
Air-side hydraulic diameter D_h [mm]	4.20624

4.3.2 The ϵ -NTU method

One of the standard methods for calculating heat exchanger performance is to use the effectiveness-number of transfer units ($\epsilon - NTU$) method, which can be found in several textbooks and publications ([14], [15]). This method has been implemented in Python and its application to the ICD duct heat exchanger will be described below:

1. Defining dimensions

Define dimensions of the heat exchanger in order to calculate total heat exchanger volume and surface areas. In this report the conical heat exchanger is treated as a rectangular box (Figure 29) with dimensions which result in exactly the same volume, cross-sectional area, and cross-sectional dimensions as the integrated heat exchanger.

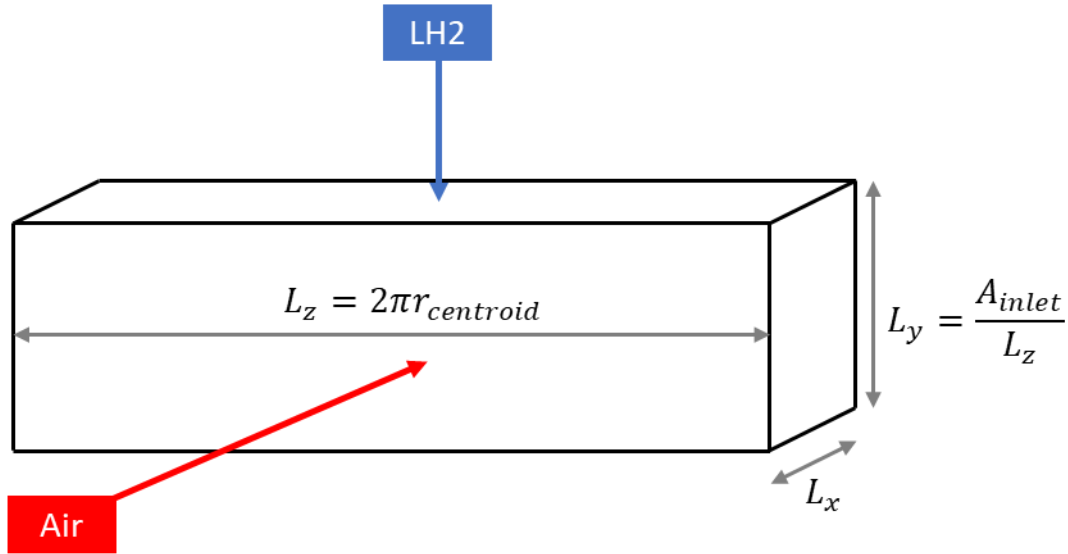


Figure 29 – Dimensions of the heat exchanger for conceptual design.

At this stage initial guesses for the heat exchanger effectiveness ϵ and pressure drops are set which allows calculating estimates for the outlet conditions of the heat exchanger. Inlet conditions are denoted by subscript 1 and outlet conditions by the subscript 2. First the definition of effectiveness:

$$\epsilon = \frac{C_{air}(T_{air,1} - T_{air,2})}{C_{min}(T_{air,1} - T_{LH2,1})} \quad (8)$$

$$C_{min} = \min(C_{air}, C_{LH2})$$

$$C_{air} = \bar{c}_{p,air} \dot{m}_{air} \quad (9)$$

$$C_{LH2} = \bar{c}_{p,LH2} \dot{m}_{LH2}$$

Re-arranging Eq. (8) yields the outlet temperature for the air side:

$$T_{air,2} = T_{air,1} - \epsilon \left(\frac{C_{min}}{C_{air}} \right) (T_{air,1} - T_{LH2,1}) \quad (10)$$

The outlet temperature of the LH2 is obtained through conservation of energy:

$$T_{LH2,2} = T_{LH2,1} + \left(\frac{C_{air}}{C_{LH2}} \right) (T_{air,1} - T_{air,2}) \quad (11)$$

This allows for calculating average thermophysical properties (denoted by a bar, e.g. \bar{c}_p) of the fluids which are evaluated at average temperatures and pressures between corresponding inlets and outlets.

2. Calculating friction factors and heat transfer coefficients

The inlet conditions for the air and hydrogen side are known from the system model as are the overall dimensions of the heat exchanger which allows calculating the Reynolds number, Nusselt number, and heat transfer coefficients for each side of the heat exchanger. Air side:

$$A_{front,air} = L_z L_y \quad (12)$$

$$G_{air} = \frac{\dot{m}}{\sigma_{air} A_{front,air}} \quad (13)$$

Where σ_{air} is the freeflow area to frontal area ratio of the air side.

$$Re_{air} = \frac{D_{h,air} G_{air}}{\bar{\mu}_{air}} \quad (14)$$

$$f = f(Re) \text{ from correlations (e.g., Figure 27)} \quad (15)$$

$$j = f(Re) \text{ from correlations (e.g., Figure 27)}$$

$$St = j/Pr^{2/3} \quad (16)$$

$$Nu_{air} = Re \cdot Pr \cdot St \quad (17)$$

$$h_{air} = \frac{Nu_{air} \cdot \bar{k}_{air}}{D_{h,air}} \quad (18)$$

Hydrogen side:

$$A_{front,LH2} = L_z L_x \quad (19)$$

$$G_{LH2} = \frac{\dot{m}}{\sigma_{LH2} A_{front,LH2}} \quad (20)$$

$$Re_{LH2} = \frac{D_{h,LH2} G_{LH2}}{\bar{\mu}_{LH2}} \quad (21)$$

Friction factor is calculated using correlations for pipe flow for the hydrogen side, using the correlation by Petukhov [16] for the turbulent region:

$$f_{laminar} = \frac{64}{Re_{LH2}} \text{ for } Re_{LH2} \leq 2000 \quad (22)$$

$$f_{turb} = (0.79 \ln Re_{LH2} - 1.64)^{-2} \text{ for } Re_{LH2} \geq 3000 \quad (23)$$

The friction factor becomes a blend of the laminar and turbulent values for the range $2000 < Re_{LH2} < 3000$. The correlation by Gnielinski [17] is used for heat transfer in pipe flow:

$$Nu_{LH2} = \frac{(f/8)(Re_{LH2} - 1000)Pr}{1 + 12.7(f/8)^{1/2}(Pr^{2/3} - 1)} \quad (24)$$

$$h_{LH2} = \frac{Nu_{LH2} \cdot \bar{k}_{LH2}}{D_{h,LH2}} \quad (25)$$

3. Calculating fin and overall surface effectiveness

First the fin effectiveness is calculated using the following relations:

$$\eta_{fin} = \frac{\tanh(mL_{fin})}{mL_{fin}} \quad (26)$$

$$m = \sqrt{\frac{2h_{air}}{k_{fin}\delta_{fin}}}$$

Where L_{fin} , k_{fin} , δ_{fin} is the fin length, thermal conductivity and thickness, respectively. Next the overall surface effectiveness of the air side can be calculated:

$$\eta_0 = 1 - \kappa_{fin}(1 - \eta_{fin}) \quad (27)$$

4. Calculating overall coefficient of heat transfer, NTUs, and HEX effectiveness

The overall heat transfer coefficient (air side) U_{air} is calculated using a thermal circuit analogy:

$$\frac{1}{U_{air}} = \frac{1}{\eta_0 h_{air}} + \frac{1}{\left(\frac{\alpha_{LH2}}{\alpha_{air}}\right) h_{LH2}} \quad (28)$$

Here it is assumed that the wall thermal resistance can be neglected and that surfaces are clean (no fouling). The term α_{air} is included in Table 24, while α_{LH2} is calculated using the tube perimeter P_{tube} and tube frontal area:

$$\alpha_{LH2} = \frac{P_{tube}}{(L_{transversal} L_{longitudinal})} \quad (29)$$

Where the is $L_{transversal}$ is the transversal spacing between each tube and $L_{longitudinal}$ is the longitudinal spacing between each tube and can be calculated using Table 24. The next step is to calculate the heat capacity rates as in Eq. (9) for each fluid flow in the heat exchanger:

$$\begin{aligned} C_{air} &= \bar{c}_{p,air} \dot{m}_{air} \\ C_{LH2} &= \bar{c}_{p,LH2} \dot{m}_{LH2} \\ C_{min} &= \min(C_{air}, C_{LH2}) \\ C_{max} &= \max(C_{air}, C_{LH2}) \end{aligned} \quad (30)$$

The number of transfer units can now be calculated:

$$N_{tu} = \frac{V_{HEX} \alpha_{air} U_{air}}{C_{min}} \quad (31)$$

The effectiveness of this heat exchanger can now be obtained from Figure 30 which relates the effectiveness of an unmixed crossflow heat exchanger with the N_{tu} and C_{min}/C_{max} . The outlet temperature for the air and LH2 sides can now be calculated using Eq. (10) and (11). The heat flow is calculated as follows:

$$Q = C_{air}(T_{air,1} - T_{air,2}) \quad (32)$$

The air-and hydrogen side pressure drops are calculated using the equations below:

$$\Delta p_{air} = \frac{G_{air}^2}{2\rho_{air,1}} \left((1 + \sigma_{air}^2) \left(\frac{\rho_{air,1}}{\rho_{air,2}} - 1 \right) + f \frac{4L_x}{D_{h,air}} \frac{\rho_{air,1}}{\bar{\rho}_{air}} \right) \quad (33)$$

$$\Delta p_{LH2} = \frac{G_{LH2}^2}{2\bar{\rho}_{LH2}} f \frac{4L_y}{D_{h,LH2}} \quad (34)$$

Now the outlet conditions and average thermophysical properties used in step 1 can be updated and the subsequent steps repeated. This is of particular importance whenever the working fluids of the heat exchanger are defined as real fluids/gases whose thermophysical properties vary with temperature and pressure.

The steps outlined in this section can be iterated to reach desired accuracy, e.g. with respect to pressure loss and/or resulting heat exchanger effectiveness.

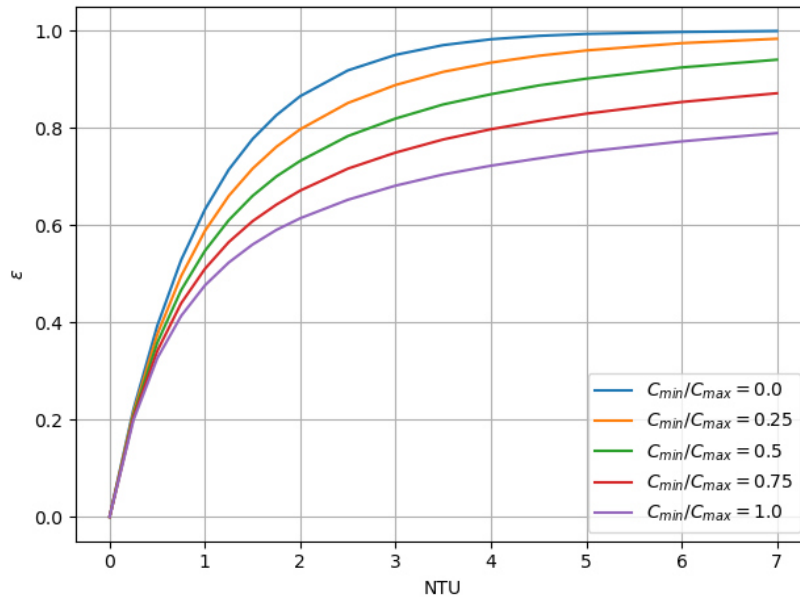


Figure 30 – Heat transfer effectiveness as function of NTUs and heat capacity ratio C_{min}/C_{max} for a crossflow heat exchanger with unmixed fluids [14].

4.3.3 Thermophysical properties

The thermophysical properties used in heat exchanger conceptual design are obtained from the National Institute of Standards and Technology (NIST) *Reference Fluid Thermodynamic and Transport Properties Database* (REFPROP) [18] via the Python wrapper for Coolprop [19]. This provides easy access to highly accurate real fluid/gas properties for the conceptual design process. In this report a *dry air mixture* has been chosen for the air side while Parahydrogen has been chosen for the hydrogen side of the heat exchanger.

4.3.4 ICD heat exchanger designs for area ratio 4 and 6

Area ratios of 4 and 6 have been chosen for the diffuser duct in the ICD since this allows for a substantial diffusion of the flow without it resulting in a prohibitively large heat exchanger and associated ducts. These area ratios together with the boundary conditions in Table 25 are inputs for the conceptual design of the heat exchanger in the ICD duct. Top-of-climb (ToC) has been chosen as the design point since it features the highest inlet Mach number for the diffuser duct (i.e. LPC outlet Mach number), while take-off (TO) and cruise are run as off-design points.

Table 25 – Boundary conditions for the ICD duct extracted from baseline engine system model

Operating point:	TO	ToC (DP)	Cruise
Mass flow [kg/s]	28.86	12.91	11.25
LPC outlet area [m^2]	0.0807	0.0807	0.0807
Air LPC outlet Mach number	0.3831	0.3997	0.3819
p_0 [Pa]	290878	118947	105723
T_0 [K]	398.2	356.7	344.1
Operating point:	TO	ToC (DP)	Cruise
Fuel flow [kg/s]	0.3143	0.1278	0.1022
LH2 p_0 [Pa]	4199841	1862803	1571484
T_0 [K]	26.66	24.31	24.07

Input parameters common for all designs are specified in Table 26, including the length of the ICD duct ($\Delta R/L$), the number of tube banks in the air flow direction, geometric scale factor for the heat exchanger geometry, and the metal thermal conductivity of the heat exchanger. The geometric scale factor is set to 0.5 which results in an isometric scaling of the entire heat exchanger geometry, in principle decreasing the air-side Reynolds number by 50% and increasing the Nusselt number and heat transfer coefficient (see Figure 27). Early calculations (not shown) showed that using the original, unscaled heat exchanger fin and tube geometry led to significantly lower heat flows (in the order of 50%) for the same heat exchanger volume.

Table 26 - Common input parameters for the compact heat exchanger designs.

$\Delta R/L$	0.15
N_{banks}	8
Geometric scale factor	0.5
Solid material (Alu 2219) thermal conductivity [W/m K]	120

The chosen designs for the area ratios 4 and 6 are presented in Table 27 and achieved core air temperature drops of more than 40 K for top-of-climb, while the design for AR 6 exceeded 50 K during take-off. As expected, the air-side pressure losses decrease with increasing area ratio, as does the hydrogen pressure loss due to increased LH2 tube length.

Table 27 – Aerothermal performance for the ICD compact heat exchangers with area ratio 4 and 6. Note that pressure losses are for the heat exchanger only and excludes the connecting ducts. Weight is only for the heat exchanger tube and fins. DP denotes design point.

Design	AR	OP	Q [kW]	L_x [m]	L_y [m]	$\Delta T_{0,air}$	$\Delta T_{0,LH2}$	Δp_{air}	Δp_{LH2}	W [kg]	ϵ
AR4B	4	ToC (DP)	520.3	0.0803	0.2116	-40.0	253.3	2.484%	0.030%	7.40	78.82%
		TO	1333.7	0.0803	0.2116	-45.7	264.9	1.782%	0.030%	7.40	73.54%
		Cruise	362.4	0.0803	0.2116	-32.0	218.8	2.440%	0.018%	7.40	70.52%
AR6D	6	ToC (DP)	565.9	0.0803	0.3175	-43.5	277.1	1.277%	0.047%	11.10	86.23%
		TO	1475.6	0.0803	0.3175	-50.5	295.2	0.863%	0.050%	11.10	81.95%
		Cruise	398.3	0.0803	0.3175	-35.1	241.7	1.260%	0.026%	11.10	77.89%

4.3.5 Duct shape optimization

For the heat exchanger to operate under optimal conditions with respect to heat transfer and pressure drop the diffuser duct needs to diffuse the flow in a uniform manner while keeping its pressure losses to a minimum. The flow entering the heat exchanger should be as uniform as possible in order to minimize the internal heat exchanger pressure loss and to avoid non-uniform cooling (i.e. cold spots). Downstream of the heat exchanger the contraction needs to guide the flow to the HPC exit while also minimizing its own pressure loss. The optimization problem can therefore be stated as follows:

- Minimize the sum of the pressure losses in the diffuser and the contraction.
- Minimize the non-uniformity ψ of the velocity entering the heat exchanger inlet:

$$\psi = \frac{\int_{A_{inlet}} \frac{1}{2} v'^2 dA}{\int_{A_{inlet}} \frac{1}{2} V^2 dA} \quad (35)$$

$$v' = V - \int_{A_{inlet}} V dA \quad (36)$$

The flow perturbation v' on the heat exchanger inlet is defined as the difference between the velocity at a specific point the inlet and the average velocity on the inlet surface (C13 in Figure 31). The last objective function is to minimize the surface area of the diffuser and contraction in order to decrease mass.

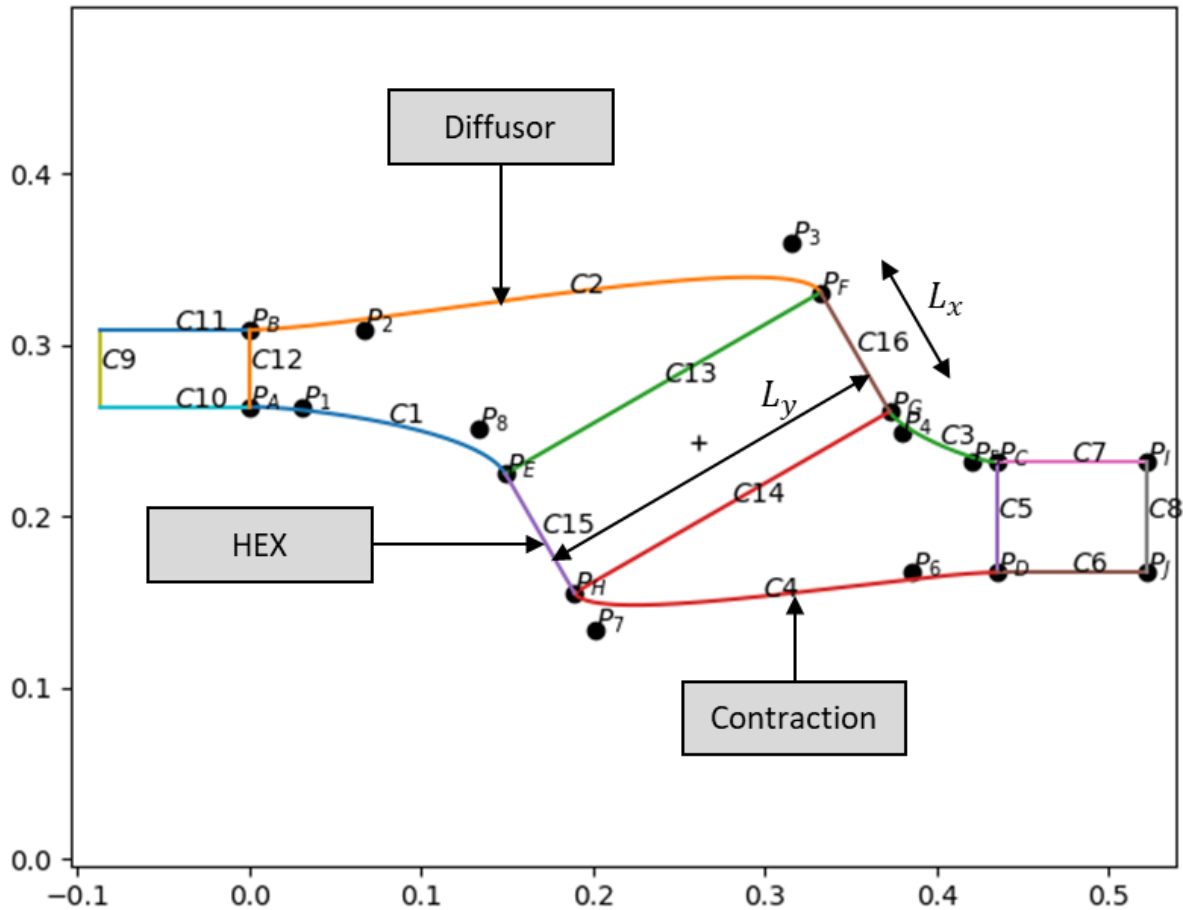


Figure 31 – Meridional view of a heat exchanger with AR 4 integrated into the ICD duct. The hub and shroud contours for the diffusor and contraction are constructed using Bézier curves.

The duct shape optimization is carried out for the three heat exchanger designs in Table 27 using the Chalmers in-house optimization platform described in [20]-[22] which is based on the NSGA-II algorithm. The optimization is initiated by performing a Latin Hypercube Sampling (LHS) of the design space which is then used to create a meta-model by means of Radial Basis Functions (RBF). The meta-model is in turn used by the genetic algorithm to find new optimal designs. After a number of generations, the 20 best cases are chosen and simulated using CFD and added to the meta-model database.

The geometry used in the CFD simulations is parametrized using Bézier curves as shown in Figure 31, whose control points are manipulated by the GA to obtain new designs. In total 19 design variables are required to define the geometry, and includes three parameters which regulate the axial position, radial position, and inclination of the heat exchanger in the duct.

Meshing is carried out using Pointwise and produces an unstructured tetrahedral mesh with hexahedral cells along the hub and shroud contours, with a first wall node height resulting in an average y^+ well below 1.

The CFD software ANSYS Fluent is used for simulating the flow with following major settings:

- 2D axisymmetric
- $k - \omega$ SST turbulence model
- Air set as an ideal gas
- Pressure inlet with total temperature and total pressure corresponding to the top-of-climb conditions in Table 25.
- Massflow outlet which targets the mass flow for the top-of-climb operating point.
- The effects of the heat exchanger on the flow:
 - The pressure drop is incorporated by imposing an inertial resistance factor K in the HEX domain (Figure 31). This factor acts in the direction normal to the inlet face of the heat

exchanger (Eq. (37)). A value several orders of magnitude greater is also imposed in the transversal direction, thereby forcing the flow along the direction of the fins of the heat exchanger.

$$K = \frac{\Delta p_{air}}{\frac{1}{2} \rho_{1,air} v_{1,air}^2 L_x} \quad (37)$$

$$v_{1,air} = \frac{\dot{m}_{air}}{A_{inlet} \rho_{1,air}}$$

- Heat transfer is incorporated into the CFD model by using an energy source term [W/m³] that acts as heat sink in the HEX domain:

$$\dot{q} = \frac{Q}{L_x L_y L_z} \quad (38)$$

The two optimizations (one for each HEX design in Table 27) were run for 100 iterations each, where each iteration corresponds to an update to the meta-models using CFD. In total, 2420 designs were simulated in CFD for each one of the optimizations. The overall results from the optimizations in terms of pressure loss and flow non-uniformity are shown in Figure 32 and Figure 33 for the two exchanger concepts. Here it can be seen that a higher diffuser area ratio AR leads to a higher pressure loss and flow non-uniformity, especially since the overall axial length of the ducts has been kept constant for all cases ($\Delta R/L = 0.15$ in Table 26).

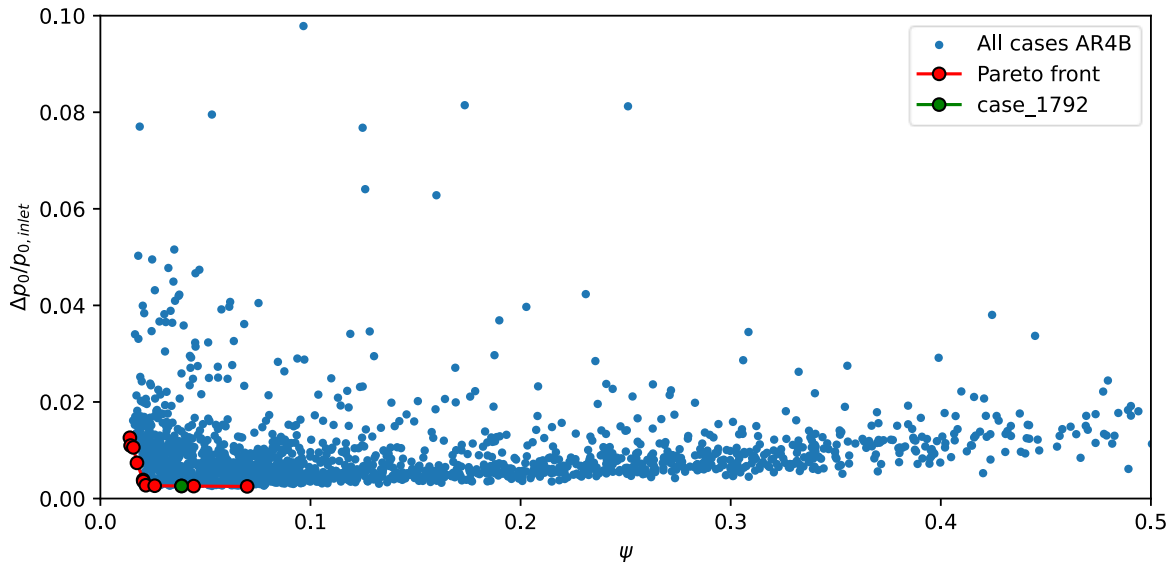


Figure 32 - Optimization results for AR4B ducts. The blue dots constitute the results of all the CFD cases run while the red dots and line represents the Pareto front for these two objective functions (pressure loss and flow non-uniformity ψ). One case (green dot) has also been chosen for each optimization for the sake of comparison.

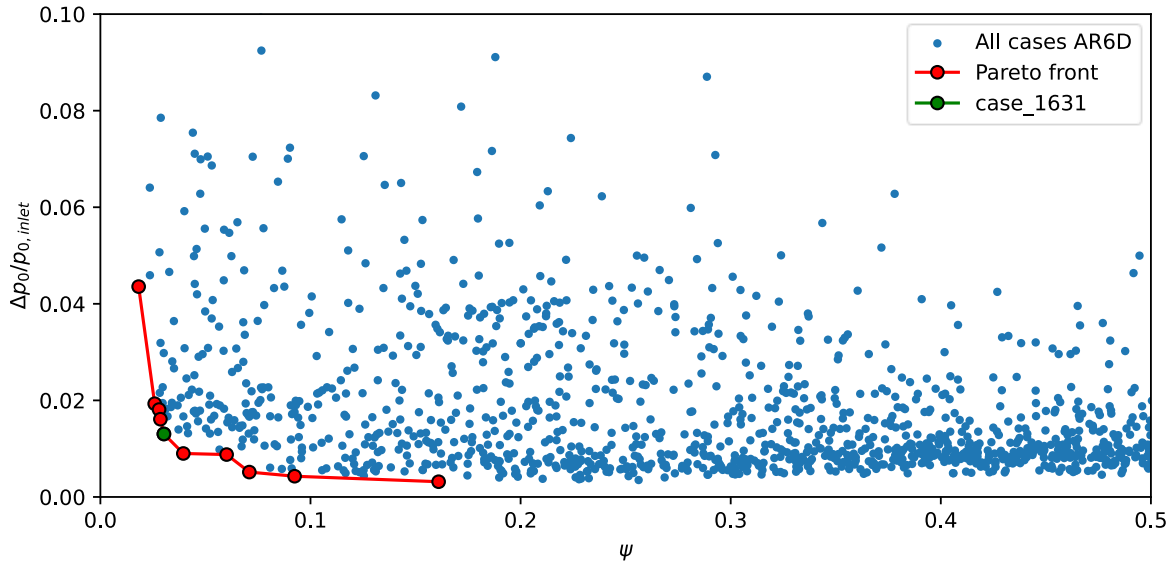


Figure 33 – Optimization results AR6D ducts. The blue dots constitute the results of all the CFD cases run while the red dots and line represents the Pareto front for these two objective functions (pressure loss and flow non-uniformity ψ). One case (green dot) has also been chosen for each optimization for the sake of comparison.

For the sake of comparison two duct cases which feature similar flow non-uniformities have been chosen from the pareto front of each optimization in Figure 32 and Figure 33 whose pressure drop breakdown is shown in Table 28. The overall pressure drop is lower for the AR6 case, and this is primarily due to the lower velocities at the inlet of the HEX for this case. For these cases the HEX is inclined and therefore the flow has a certain incidence relative to the inlet of the HEX, which means that the kinetic energy of the transversal velocity of the incoming flow will become a loss as well. The diffuser and contraction pressure losses are relatively small, while the pressure drop inside the HEX along the air direction of the HEX (along L_x) shows good agreement with the pressure loss obtained from conceptual design (Table 27).

Table 28 – Flow non-uniformity and pressure losses for the chosen cases from the optimizations.

	AR4B_1792	AR6D_1631
ψ	3.863%	3.024%
$\Delta p_{0,total}/p_{0,inlet}$	7.240%	4.289%
$\Delta p_{0,diffusor}/p_{0,inlet}$	0.203%	0.333%
$0.5\rho V_{trans}^2/p_{0,HEX,inlet}$	4.428%	2.650%
$\Delta p_{0,HEX}/p_{0,inlet}$	2.465%	1.160%
$\Delta p_{0,contraction}/p_{0,inlet}$	0.145%	0.147%

Figure 34 to Figure 35 display the total pressure, total temperature, and velocity fields for the chosen cases from the optimizations. It is evident that the flow diffuses relatively well for the AR4B_1792 case but becomes slightly worse for the AR6D_1631 case. The flow in the contractions does not seem to feature any flow separation, but instead relatively high flow velocities are found the hub and shroud corners adjacent to the outlet which flows into the HPC. The temperature fields are relatively uniform along the height of HEX, indicating uniform cooling of the flow.

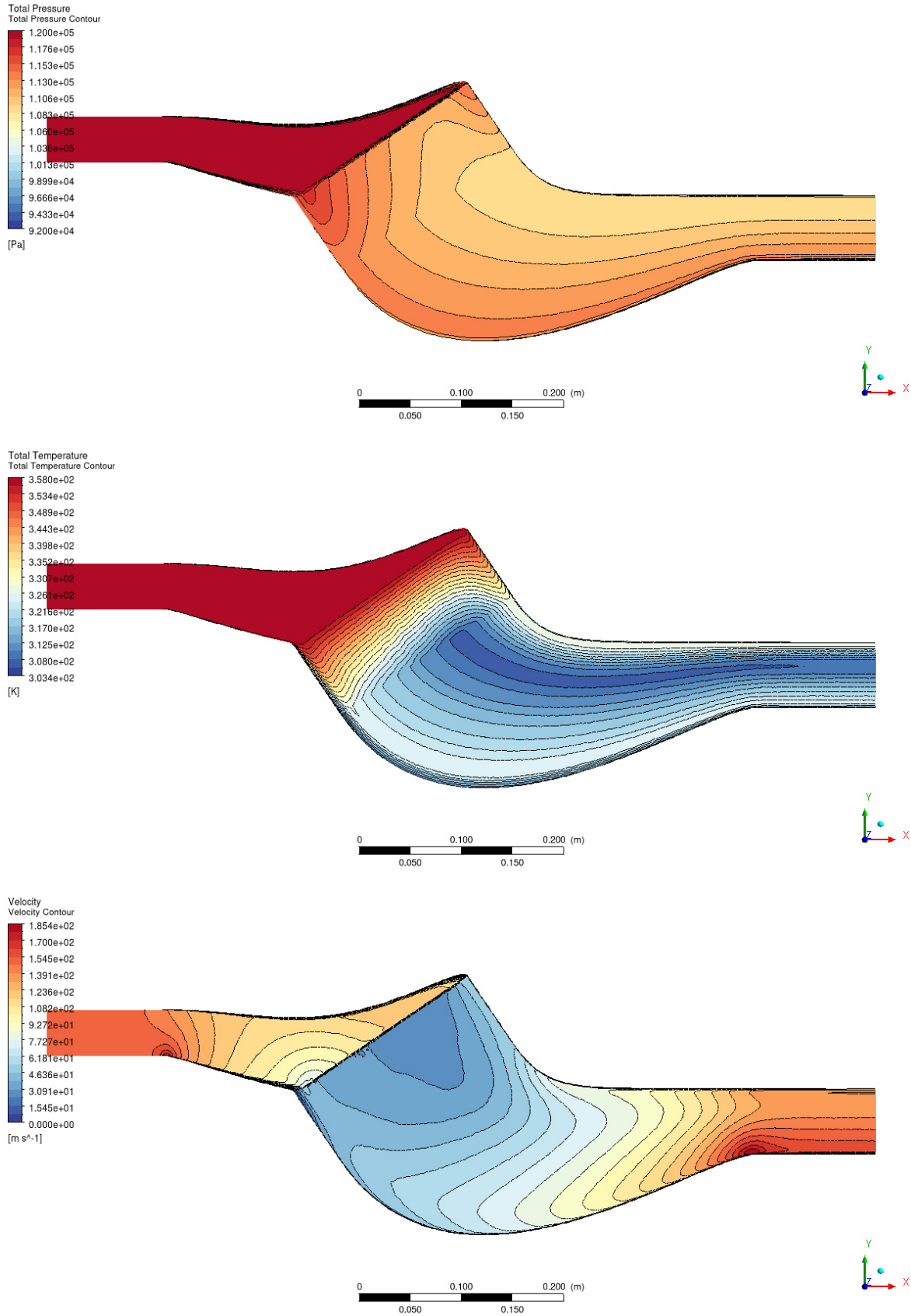


Figure 34 – CFD results for the AR4B_1792 heat exchanger and connecting ducts. Top: Total pressure, Center: Total Temperature, Bottom: Velocity.

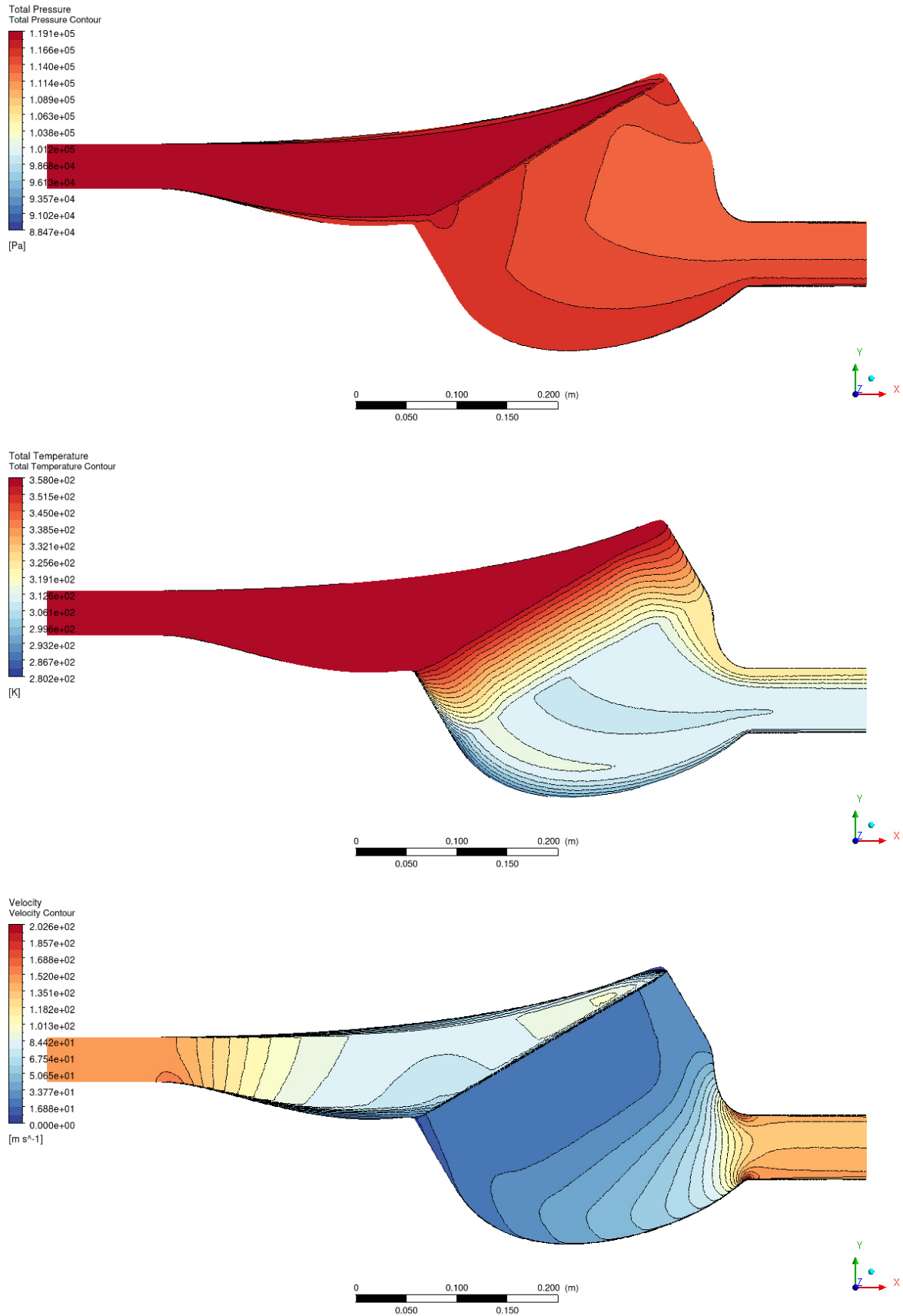


Figure 35 - CFD results for the AR6D_1631 heat exchanger and connecting ducts. Top: Total pressure, Center: Total Temperature, Bottom: Velocity.

Additional optimization could potentially further improve aerothermal performance but at an increased computational cost and diminished improvements in performance. The cases presented here show relatively good aerothermal performance but there is a potential for decreasing the axial length of the AR4B geometry. This has been carried out through an additional optimization where the diffuser of the AR4B_1792 case has been kept fixed while varying the length and shape of the contraction. The resulting geometry (AR4B_C436) has a slightly higher total pressure loss due to larger transversal velocity losses but is 35% shorter. The geometry and velocity for this design is shown in Figure 36.

The AR4B_C436 and AR6D_1631 geometries will be used for generating pressure loss correlations for system-level studies.

Table 29 - Flow non-uniformity and pressure losses for the new case with shorter contraction and previous cases.

	AR4B_C436	AR4B_1792	AR6D_1631
ψ	4.743%	3.863%	3.024%
$\Delta p_{0,total}/p_{0,inlet}$	7.930%	7.240%	4.289%
$\Delta p_{0,diffusor}/p_{0,inlet}$	0.219%	0.203%	0.333%
$0.5\rho V_{trans}^2/p_{0,HEX,inlet}$	5.005%	4.428%	2.650%
$\Delta p_{0,HEX}/p_{0,inlet}$	2.593%	2.465%	1.160%
$\Delta p_{0,contraction}/p_{0,inlet}$	0.113%	0.145%	0.147%
Axial length [m]:	0.375	0.580	0.580
	(new)		

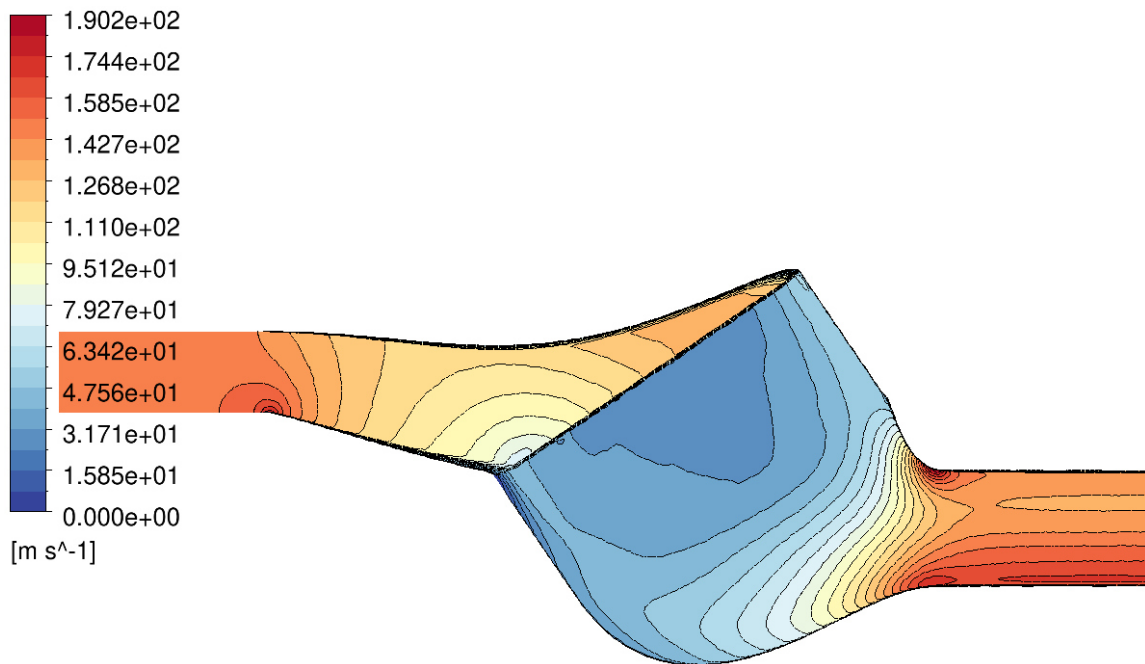


Figure 36 – Velocity field for the AR4B_C436 case.

4.3.6 Pressure loss correlations

The pressure losses in the diffuser and contraction duct have been extracted for a series of duct Reynolds numbers in order to generate pressure loss correlations for system-level studies. This has been carried out by using the CFD simulations from section 4.3.5 and varying the dynamic viscosity. For the diffuser a total pressure loss coefficient $K_{diffuser}$ has been defined which consists of two terms, the first (K_{diff}) representing the pressure loss in the diffuser itself and the second term (K_{trans}) representing the pressure loss due to the transversal velocity component present at the inlet of the heat exchanger:

$$K_{diffuser} = \frac{p_{02} - p_{01}}{p_{01} - p_1} = K_{diff} + K_{trans} = \frac{p_{01b} - p_{01}}{p_{01} - p_1} + \frac{\rho_{1b} V_{1b,trans}^2}{2(p_{01} - p_1)} \quad (39)$$

Here station 1 refers to the diffuser inlet, station 1b to a position just upstream of the diffuser outlet, and station 2 at the diffuser outlet, which assumes that all the kinetic energy of the transversal velocity has become a loss. For the contraction a factor is used which relates the total pressure loss to the dynamic pressure:

$$K_{contr} = \frac{p_{03} - p_{04}}{p_{03} - p_3} \quad (40)$$

Where stations 3 and 4 denote the inlet and outlet of the contraction duct. The obtained correlations for the AR4B_C436 geometry are stated in Eq. (41) to (43). Plots of the of the underlying data and the correlations are plotted in Figure 37 and Figure 38.

$$K_{diff} = 0.1281 Re_{D_{h,diff}}^{-0.1191} + \frac{560.7}{Re_{D_{h,diff}}} \quad (41)$$

$$K_{trans} = 0.5100 Re_{D_{h,diff}}^{-0.004336} + \frac{259.4}{Re_{D_{h,diff}}} \quad (42)$$

$$K_{contr} = 0.4776 Re_{D_{h,contr}}^{-0.06259} + \frac{15527}{Re_{D_{h,contr}}} \quad (43)$$

Eq. (41) to Eq. (43) have maximum errors of 0.33%, 0.03%, and 3.08% respectively. The Reynolds number used in (41) and (42) is based on the radii of the diffuser inlet. For the contraction pressure loss the Reynolds number is instead based on the radii of the contraction outlet. The range of validity for the diffuser correlations is $5 \cdot 10^4 < Re_{D_{h,diff}} < 3 \cdot 10^6$ while for the contraction it is $7 \cdot 10^4 < Re_{D_{h,contr}} < 4 \cdot 10^6$.

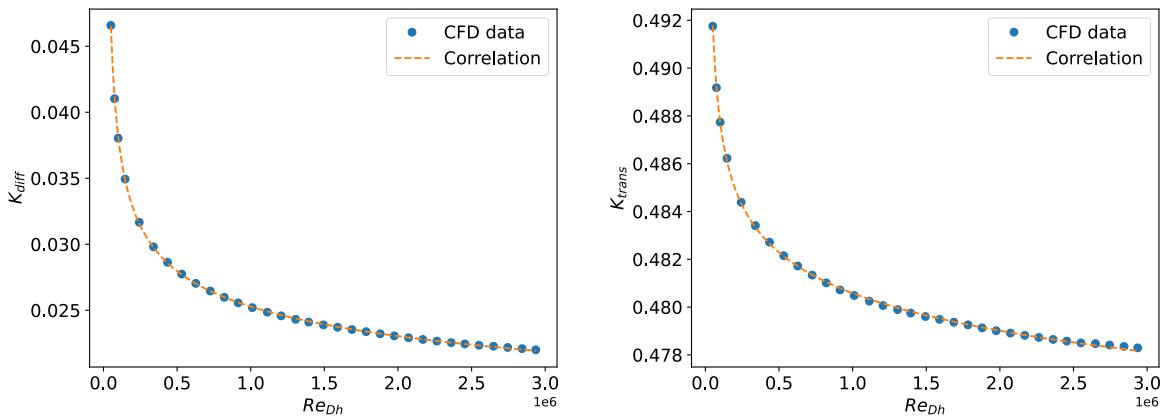


Figure 37 – Diffuser total pressure loss factor K_{diff} and transversal velocity loss K_{trans} for the AR4B_C436 diffuser geometry. Each point is a CFD simulation while the dotted line is the extracted correlation.

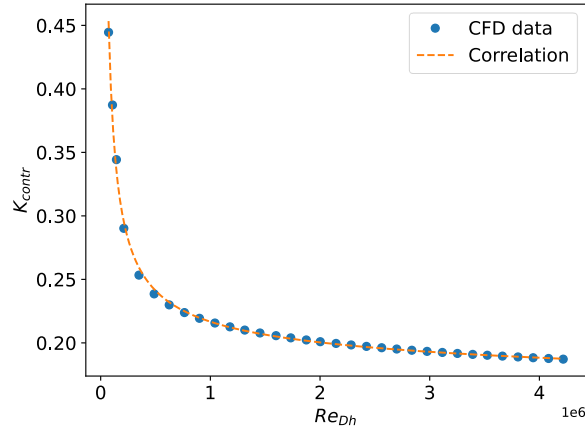


Figure 38 - Total pressure loss factor K_{contr} for the AR4B_C436 contraction geometry. Each point is a CFD simulation while the dotted line is the extracted correlation. Note that the total pressure loss is normalized with the contraction intake dynamic pressure and not the highest value across the duct.

The obtained correlations for the AR6D_1631 geometry are stated in Eq. (44) to (46). Plots of the of the underlying data and the correlations are plotted in Figure 39 and Figure 40.

$$K_{diff} = 0.1321Re_{Dh,diff}^{-0.1395} + \frac{1154}{Re_{Dh,diff}} \quad (44)$$

$$K_{trans} = 0.2915Re_{Dh,diff}^{-0.00737} + \frac{275.1}{Re_{Dh,diff}} \quad (45)$$

$$K_{contr} = 1.546Re_{Dh,contr}^{-0.0908} + \frac{40797}{Re_{Dh,contr}} \quad (46)$$

Eq. (44) to (46) have a maximum error of 2.64%, 0.31%, and 5.1% . The range of validity for the diffuser correlations is $5 \cdot 10^4 < Re_{Dh,diff} < 3 \cdot 10^6$ while for the contraction it is $7 \cdot 10^4 < Re_{Dh,contr} < 4 \cdot 10^6$.

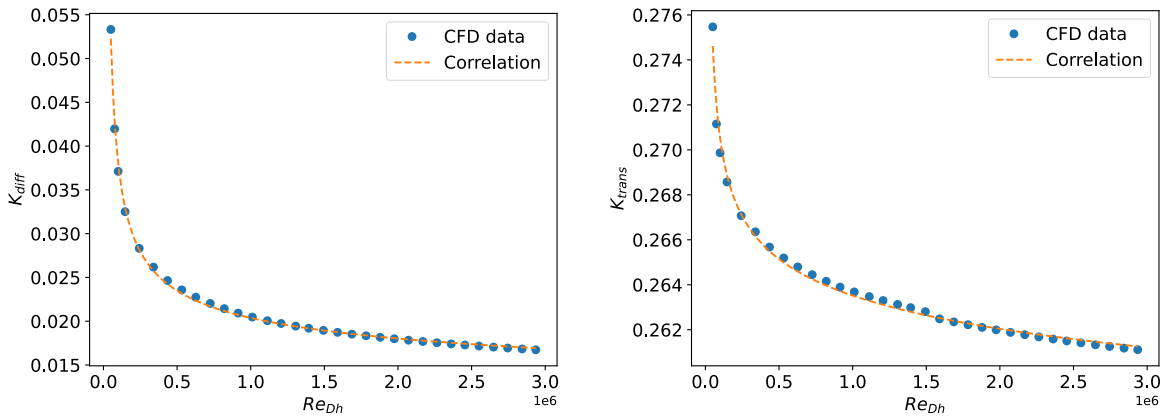


Figure 39 – Diffuser total pressure loss factor K_{diff} and transversal velocity loss K_{trans} for the AR6D_1631 diffuser geometry. Each point is a CFD simulation while the dotted line is the extracted correlation.

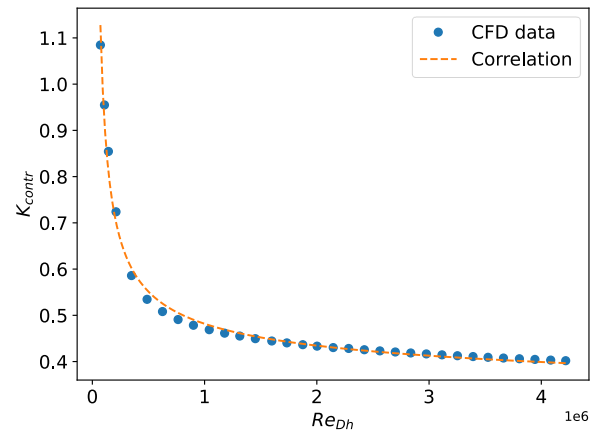


Figure 40 – Total pressure loss factor K_{contr} for the AR6D_1631 contraction geometry. Each point is a CFD simulation while the dotted line is the extracted correlation. Note that the total pressure loss is normalized with the contraction intake dynamic pressure and not the highest value across the duct.

4.3.7 TRS heat exchanger conceptual design

The methodology used for the ICD compact heat exchanger can also be applied on a TRS heat exchanger. The boundary conditions and input parameters used for the design are included in Table 30 and Table 31. Calculations have been carried out for AR 4 and 6, and for two fractions of core air flow (25% and 50%). Two additional cases have also been carried out which represent an intercooled-recuperated setup and where the hydrogen is assumed to have passed through an ICD heat exchanger before being routed through the TRS heat exchanger, thereby resulting in an increased LH2 inlet temperature. The results shown in Table 32 to Table 33 seem to indicate that on average the pressure drop of the AR 6 heat exchangers amounts to half of the pressure drop of the AR 4 designs. The highest effectiveness is reached for the 50% core air flow, while the AR 4 and AR 6 designs deliver a similar amount of heat flow for the cases representing an intercooled-recuperated setup.

The material used for these calculations is Aluminium 2219 which can become problematic for the air-side temperature ranges experienced by the TRS HEX. Therefore, an additional calculation was carried out for AR 4 using a thermal conductivity of 10 [W/m K] and a density of 8070 [kg/m³], roughly corresponding to the steel alloy NASA-HR-1, which has excellent hydrogen embrittlement resistance [23]. The results indicate a decrease in heat flow of approximately 10% and similar air side pressure drops.

Table 30 – Boundary conditions for the TRS duct extracted from baseline engine system model.

Operating point:		TO	ToC (DP)	Cruise
Air	Mass flow [kg/s]	28.86	12.91	11.25
	LPC outlet area [m ²]	0.3315	0.3315	0.3315
	LPC outlet Mach number	0.3281	0.52	0.4228
	p_0 [Pa]	123497	39247	34967
	T_0 [K]	847.5	720.0	683.7
Operating point:		TO	ToC (DP)	Cruise
LH2	Fuel flow [kg/s]	0.3143	0.1278	0.1022
	p_0 [Pa]	4199841	1862803	1571484
	T_0 [K]	26.66	24.31	24.07
Operating point:		TO	ToC (DP)	Cruise
LH2 (interc./recup.)	AR4 T_0	291.5	277.4	242.9
	AR6 T_0	321.8	301.4	265.8

Table 31 - Common input parameters for the compact heat exchanger designs.

$\Delta R/L$	0.15
N_{banks}	8
Geometric scale factor	0.5
Solid material (Alu 2219) thermal conductivity [W/m K]	120

Table 32 - Aerothermal performance for compact heat exchangers with area ratio 4 for the TRS. Note that pressure losses are for the heat exchanger only and exclude the connecting ducts. Weight only includes the heat exchanger tube and fins. DP denotes design point. The case AR4TRS_50W constitutes a case where the hydrogen has passed through a heat exchanger in the ICD before reaching the TRS heat exchanger and has inlet temperatures according to AR4 T_0 in Table 30.

Design	AR	OP	Q [kW]	L_x [m]	L_y [m]	$\Delta T_{0,air}$	$\Delta T_{0,LH2}$	Δp_{air}	Δp_{LH2}	W [kg]	€
AR4TRS-50 (50% of core air flow)	4	ToC (DP)	1139.8	0.0803	0.3582	-150.6	584.8	6.217%	0.073%	15.20	0.8425
		TO	3155.8	0.0803	0.3582	-186.5	661.4	2.186%	0.096%	15.20	0.8066
		Cruise	914.8	0.0803	0.3582	-138.6	587.0	6.164%	0.082%	15.20	0.8913
AR4TRS-25 (25% of core air flow)	4	ToC (DP)	766.6	0.0803	0.1907	-202.6	384.1	5.797%	0.022%	7.60	0.5534
		TO	2247.6	0.0803	0.1907	-265.7	463.1	1.955%	0.039%	7.60	0.5647
		Cruise	655.4	0.0803	0.1907	-198.6	412.5	5.677%	0.027%	7.60	0.6264
AR4TRS_50W (50% of core air flow)	4	ToC (DP)	732.1	0.0803	0.3582	-96.7	391.9	6.655%	0.143%	15.20	0.8891
		TO	1964.7	0.0803	0.3582	-116.1	427.5	2.392%	0.110%	15.20	0.7702
		Cruise	608.4	0.0803	0.3582	-92.2	405.7	6.543%	0.145%	15.20	0.9227

Table 33 - Aerothermal performance for compact heat exchangers with area ratio 6 for the TRS. Note that pressure losses are for the heat exchanger only and exclude the connecting ducts. Weight only includes the heat exchanger tube and fins. DP denotes design point. The case AR6TRS_50W constitutes a case where the hydrogen has passed through a heat exchanger in the ICD before reaching the TRS heat exchanger and has inlet temperatures according to AR6 T_0 in Table 30.

Design	AR	OP	Q [kW]	L_x [m]	L_y [m]	$\Delta T_{0,air}$	$\Delta T_{0,LH2}$	Δp_{air}	Δp_{LH2}	W [kg]	€
AR6TRS-50 (50% of core air flow)	6	ToC (DP)	1236.5	0.0803	0.4969	-163.4	636.7	3.414%	0.106%	22.81	0.9161
		TO	3379.6	0.0803	0.4969	-199.7	710.1	1.188%	0.125%	22.81	0.8654
		Cruise	966.1	0.0803	0.4969	-146.4	621.4	3.216%	0.115%	22.81	0.9428
AR6TRS-25 (25% of core air flow)	6	ToC (DP)	918.0	0.0803	0.2633	-242.6	465.5	3.095%	0.037%	11.40	0.6698
		TO	2527.8	0.0803	0.2633	-298.8	524.3	1.046%	0.053%	11.40	0.6390
		Cruise	755.3	0.0803	0.2633	-228.9	479.8	2.894%	0.043%	11.40	0.7278
AR6TRS_50W (50% of core air flow)	6	ToC (DP)	735.2	0.0803	0.4969	-97.1	394.2	3.681%	0.200%	22.81	0.9433
		TO	1933.4	0.0803	0.4969	-114.3	421.3	1.311%	0.113%	22.81	0.8021
		Cruise	600.1	0.0803	0.4969	-90.9	401.3	3.434%	0.201%	22.81	0.9615

Table 34 - Aerothermal performance for a compact heat exchanger with an area ratio 4 for the TRS and steel as the structural material.

Design	AR	OP	Q [kW]	L_x [m]	L_y [m]	$\Delta T_{0,air}$	$\Delta T_{0,LH2}$	Δp_{air}	Δp_{LH2}	W [kg]	€
AR4TRS-50S (50% of core air flow, steel)	4	ToC (DP)	1058.1	0.0803	0.3582	-139.8	540.9	6.304%	0.064%	43.20	0.7792
		TO	2770.2	0.0803	0.3582	-163.7	577.3	2.253%	0.083%	43.20	0.7040
		Cruise	860.9	0.0803	0.3582	-130.5	550.7	6.230%	0.074%	43.20	0.8363

5 Integrated performance and engine conceptual design

The present section reports on compact heat exchanger engine integration and performance studies. The usage of existing turbomachinery surfaces will not be addressed due to the limited heat transfer rates that are not expected to have major impact on cycle performance.

5.1 Integrated performance

The models that simulate the aerothermal performance of the compact finned tubed heat exchangers and ducts are integrated into GESTPAN for engine performance studies. Parahydrogen is modeled using REFPROP [18] to account for temperature-pressure variation in properties in the heat exchangers and fuel system. The combustion gas properties are modeled using splines generated with CEA (NASA Chemical Equilibrium with Applications) [24], for varying fuel air ratio, inlet enthalpy and pressure. More details about the methods used to simulate the hydrogen engines can be found in the ENABLEH2 public deliverable 2.1 [25].

5.1.1 Intercooled engines

The computed performance for two different intercooler designs, previously reported in section 4.3.4, is listed in Table 35. The baseline cycle performance, reported in Table 2, is mostly retained and the pressure ratio of the LPC is increased to compensate for the pressure loss across the newly added ducts and heat exchanger. The low-pressure system was rematched to the new core by increasing the BPR and keeping the fan pressure ratio constant until the same velocity ratio (V_{18}/V_8) (V_{18} – cold exhaust velocity, V_8 – hot exhaust velocity) was achieved. The obvious differences, relative to the baseline cycle, are a decrease in HPC outlet temperature due to the reduction of core air temperature in the intercooler, increase in BPR due to an increase in core specific power, and an increase in fuel temperature due to the pre-heating of fuel in the intercooler. Specific fuel consumption is therefore mainly affected by a change in fuel enthalpy due to pre-heating and penalized by the pressure losses associated with the inclusion of new ducts and heat exchangers. In general for the proposed designs we see a net reduction in SFC. One might argue that this analysis does not allow to fully quantify the potential of intercooling on cycle performance. Intercooling allows for reduced temperatures at similar OPR levels, opening for the possibility of further increasing the pressure ratio until temperature limitations or scale effects on component efficiencies deny further improvements. This was not addressed in the present report. Nevertheless, the provided data sets a baseline level for further intercooling studies, where the full extent on cycle performance can be quantified. Regarding NOx emissions it is observed that intercooling allows to reduce EINOx by about 12% to 33% or 16% to 40% depending on the intercooler design and operating point.

Table 35 – Performance data for the intercooled LH2 engine concepts.

	Intercooled AR4			Intercooled AR6		
	MTO	MCL	Mid-Cruise	MTO	MCL	Mid-Cruise
Altitude (ft)	0	35000	35000	0	35000	35000
Mach Number	0	0.75	0.75	0	0.75	0.75
Net Thrust (lbs)	30,600	6,290	5,050	30,600	6,290	5,050
DT_{ISA} (K)	0	0	0	0	0	0
Intercooler effectiveness	0.73	0.77	0.67	0.82	0.84	0.77
Intercooler pressure loss	4.4%	4.8%	4.7%	2.2%	2.5%	2.5%
T3 (K)	784	720	702	768	707	687
P3 (bar)	41.0	17.5	14.7	41.0	17.5	14.7
T4 (K)	1825	1700	1635	1825	1705	1633
BPR	18.6	18.1	20.1	18.8	18.4	20.3
FPR	1.44	1.54	1.45	1.44	1.54	1.45
OPR	40.5	50.2	42.3	40.5	50.2	42.3
T_{fuel} (K)	303	287	244	333	306	276
SFC (mg/Ns)	2.28	4.51	4.52	2.27	4.49	4.49
Δ SFC (relative to baseline)	-3.0%	-2.4%	-1.5%	-3.4%	-2.6%	-2.2%

	Intercooled AR4			Intercooled AR6		
	MTO	MCL	Mid-Cruise	MTO	MCL	Mid-Cruise
EINOx	26.8	11.5	8.4	24.0	11.2	8.1
ΔEINOx (relative to baseline)	-33%	-27%	-12%	-40%	-30%	-16%

5.1.2 Intercooled-recuperated and recuperated engines

The performance data computed for the intercooled – recuperated and intercooled engines is listed in Table 36. Once again, the baseline cycle performance, reported in Table 2, is mostly retained. In contrast to the intercooler, the recuperator only uses about half of the core flow and ejects the cooler exhaust gas through a separate nozzle. The thrust is therefore generated by the cold nozzle, hot nozzle and recuperator exhaust nozzle. This introduces another degree of freedom in the optimization, i.e. the relative amount of core air that is used to pre-heat the fuel in the exhaust. For the intercooled – recuperated concept the pressure ratio in the LPC is increased to compensate for the pressure loss across the intercooler just to maintain the cycle OPR. Again, the low-pressure system is rematched to the new core by increasing the BPR and keeping the fan pressure ratio constant until the baseline velocity ratio is achieved. When compared to the baseline engine the major differences in the intercooled-recuperator concept can once again be observed in the decrease in HPC outlet temperature, due to the reduction of core air temperature, increase in BPR due to an increase in core specific power, and an increase in fuel temperature due to the pre-heating of fuel in the intercooler. For the recuperated concept the main difference is the increased fuel temperature and pressure losses in the recuperator exhaust. Specific fuel consumption is therefore mainly affected by a change in fuel enthalpy due to pre-heating and penalized by the pressure losses associated with the inclusion of new ducts and heat exchangers. The reduction in SFC is substantially larger than the one provided by the intercooled concepts in Table 35, mainly at cruise. This reflects the potential of the exhaust gas in terms of heat source for the fuel, leading to significant temperature rise for an acceptable pressure loss of about 5%-9% in 50% of the core flow. In a similar fashion to the intercooled engine studies above, the present analysis does not provide the full extent of heat management potential within the hydrogen fuel system. Still, it can be used to set a baseline level for future cycle optimization studies, using the new available design parameters. Regarding NOx emissions it is observed that intercooling together with recuperation allows to reduce EINOx by about 17% to 39% whereas recuperation alone only contributes to a reduction between 9%-18% mainly driven by reductions in fuel-air ratio which lowers the combustion equivalence ratio. It should be mentioned that the correlation used for EINOx does not include the effect of fuel temperature on NOx emissions and should be investigated in more detail.

Table 36 – Performance data for the intercooled-recuperated and recuperated LH2 engine concepts.

	Intercooled AR4 – Recuperated AR4			Recuperated AR4		
	MTO	MCL	Mid-Cruise	MTO	MCL	Mid-Cruise
Altitude (ft)	0	35000	35000	0	35000	35000
Mach Number	0	0.75	0.75	0	0.75	0.75
Net Thrust (lbs)	30,600	6,290	5,050	30,600	6,290	5,050
DT _{ISA} (K)	0	0	0	0	0	0
Intercooler effectiveness	0.74	0.77	0.66	NA	NA	NA
Recuperator effectiveness	0.64	0.85	0.87	0.72	0.81	0.86
Intercooler pressure loss	4.4%	4.9%	4.8%	NA	NA	NA
BPR recuperator	1.0	0.96	0.98	1.0	0.96	0.99
Recuperator pressure loss	5.4%	8.8%	8.6%	5.4%	8.8%	8.5%
T3 (K)	788	727	708	871	797	760
P3 (bar)	41.0	17.5	14.7	41.0	17.5	14.7
T4 (K)	1825	1704	1637	1825	1694	1603
BPR	18.2	17.7	19.6	16.8	16.4	17.8

	Intercooled AR4 – Recuperated AR4			Recuperated AR4		
	MTO	MCL	Mid-Cruise	MTO	MCL	Mid-Cruise
FPR	1.44	1.54	1.45	1.44	1.54	1.45
OPR	40.5	50.2	42.3	40.5	50.2	42.3
T_{fuel} (K)	656	669	657	623	599	600
SFC (mg/Ns)	2.21	4.38	4.38	2.21	4.39	4.38
Δ SFC (relative to baseline)	-6.0%	-5.0%	-4.6%	-6.0%	-5.0%	-4.6%
EINOx	24.4	10.7	7.9	33.0	12.8	8.7
Δ EINOx (relative to baseline)	-39%	-33%	-17%	-18%	-19%	-9%

5.2 Conceptual design and impact on fuel burn

Conceptual design is carried out using the Chalmers in-house WEICO (WEIght and COst) tool. WEICO allows for an estimation of component-based weight and size of conventional turbomachinery. Additional weight models were developed for the heat exchangers. The intercooler is fabricated from aluminum AL2219, whereas the recuperator is fabricated from steel (NASA-HR1) and their weight is calculated based on the estimation of the required number of tubes and fins, internal and external pressures, and material properties. The design specifications for two heat exchangers with different inlet areas are given in Table 37. Note that for the present study, the intercooler HEX conceptual design is mostly retained and only the height varies with inlet area, hence the area available for heat transfer changes across designs and thus the performance. A concept illustration of a heat exchanger with an area ratio of six is shown in Figure 41. It should also be noted that the current fin thickness is based on the fin geometry used by Kays [14] from which experimental heat transfer pressure data is available. The fin thickness corresponds to only 3.6% of the fin spacing and could potentially be increased to match future requirements on strength, erosion, and possibly corrosion.

Both the intercooler and recuperator heat exchangers can potentially have issues with icing. Accumulation of water ice can become an issue for both, and perhaps even carbon dioxide (dry ice) if the temperatures become too low. Recirculating downstream, warm hydrogen could raise the surface temperature of the heat exchanger to avoid freezing, either continuously, or intermittently for de-icing. It should be mentioned that is a known issue for cryogenic heat exchangers which is being researched elsewhere [27].

Table 37 – Design specifications for the AR4 and AR6 heat exchangers.

	N_{tubes}	Tube cross-section dimensions [mm]	Tube thickness [mm]	N_{fins}	Fin spacing [mm]	Fin thickness [μ m]	Height [m]	Length HEX [m]	Length (inc. ducts) [m]
Intercooler AR4	1747	9.36x1.27	0.254	152	1.40	50.8	0.2116	0.0803	0.375
Intercooler AR6	1747	9.36x1.27	0.254	227	1.40	50.8	0.3175	0.0803	0.580
Recuperator AR4	2415	9.36x1.27	0.254	225	1.40	50.8	0.3144	0.0803	0.530

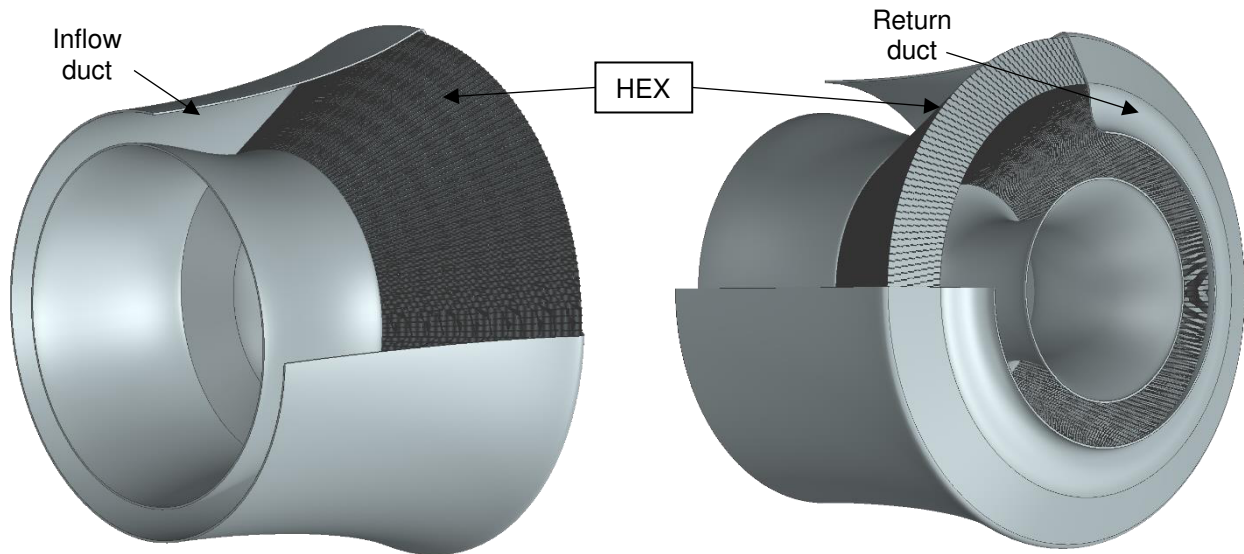


Figure 41 - Concept illustration for the AR6D_1631 heat exchanger and connecting ducts. The image to the left is where the core air flow from the LPC enters the diffuser, while the image to the right is where air exits the contraction and enters the downstream HPC.

The conceptual designs of two intercooled-geared turbofan engines, featuring different heat exchanger sizes are shown in Figure 42, whereas the intercooled-recuperated and recuperated engines are shown in Figure 43. One can observe that the fan and nacelle sizes are retained across the different architectures, and it is equal to the one estimated for the baseline engine. An important difference can be easily identified in the high-pressure system, with the stage count in the HPC decreasing with intercooling. The number of HPC stages dropped from 10 (baseline) to 8 (Intercooling AR4) and 7 (intercooling AR6). This is due to the decrease in compression work due to precooling and reduced stage loading. The larger size of the AR6 intercooler allows for a slightly larger temperature drop in the core allowing to reduce one additional stage. However, it is important to note that the HPC last stage blade height across all designs is already quite a limiting factor. To alleviate this problem, it seems possible to slightly reduce the average radius of the HPC, however this will reduce the average blade speed and increase blade loading, possibly requiring an increase in stage count.

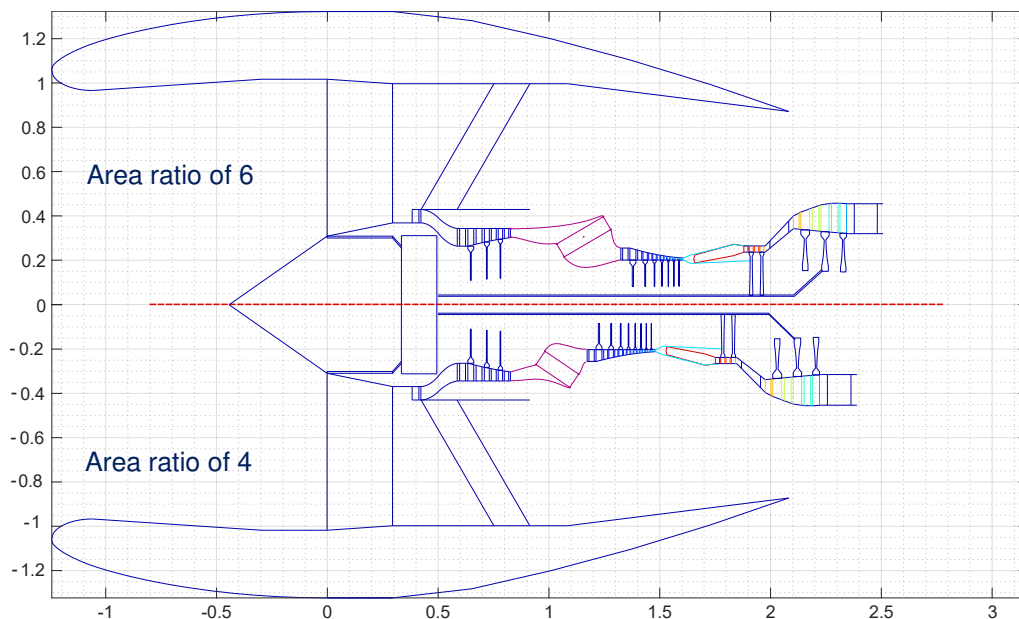


Figure 42 - Meridional cross-sectional drawing of the LH2 intercooled geared turbofan engine.

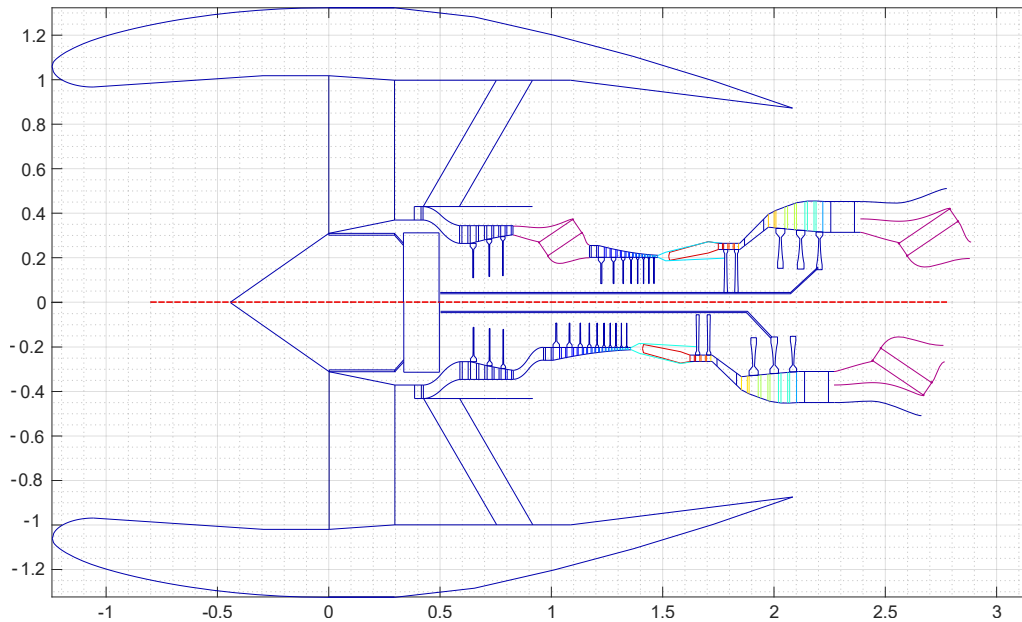


Figure 43 - Meridional cross-sectional drawing of the LH2 intercooled – recuperated engine

Table 38 summarizes the conceptual design results for all the architectures, including the impact of the heat management system on engine weight and length. The impact on variation in fuel burn relative to the baseline is given in the last three columns and it is broken down into the contribution from SFC and engine weight variation. The impact of fan diameter on engine fuel burn is negligible and therefore not shown. It is noted that the intercooled concepts seem to reduce the engine weight. This is mainly caused by the increase in core specific power and decrease in HPC stages. The added mass of the heat exchangers and ducts for the intercooled concepts amounts to a total of 49.4 kg and 81 kg for the AR4 and AR6 designs, respectively. Regarding the intercooled–recuperated concepts the added weight is about 113 kg and 160 kg for the recuperated and intercooled–recuperated engines. The highest fuel burn reduction is observed in the recuperated concept, which provides a similar SFC as the intercooled–recuperated engines but it is slightly lighter.

Table 38 – Engine mass and length for the different variants. Length is measured from fan leading edge to TRS trailing edge or recuperator exhaust.

Variant	Mass (kg)	Architecture	Mass total HEX [kg]	Mass total Hex Ducts [kg]	Length (m)	$\Delta_{FB,SFC}$	$\Delta_{FB,W}$	Δ_{FB} (3000 NM)
Baseline	3185	1+3+10+2+3	-	-	2.24	datum	datum	datum
Intercooled AR4	3127	1+3+8+2+3	7.40	42	2.4	-2.06%	-0.26%	-2.3%
Intercooled AR6	3159	1+3+7+2+3	11.1	70	2.5	-2.96%	-0.12%	-3.1%
Intercooler AR4 Recuperated AR4	3440	1+3+8+2+3	50	110	2.9	-5.94%	1.17%	-4.8%
Recuperated AR4	3390	1+3+10+2+3	43	70	2.75	-5.94%	0.93%	-5.1%

At the conceptual design level, the uncertainty of the estimated heat exchanger mass is very high. Therefore, a sensitivity study was carried out to estimate the impact of heat exchanger mass variation on aircraft fuel burn performance, the result is shown in Figure 44. An increase in heat exchanger masses (including ducts) for the intercooled-recuperated engine of 50% (increase to 240 kg) will lead to an increase in fuel burn of about 0.5 percentage points. Other variations can be easily calculated using the aircraft trade factors presented in section 3.2.

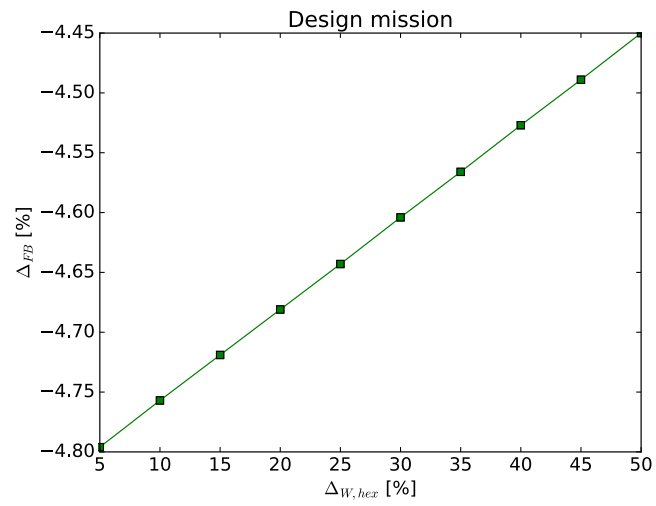


Figure 44 – Impact on heat exchanger mass variation (including ducts) on fuel burn for the design mission.

6 Conclusions

- Aircraft and engine system models were generated in order to provide a baseline concept for which intercooling and recuperation studies could be carried out.
- Intercooling:
 - Existing aero surfaces can be used for heat transfer, albeit achieving relatively low heat flows. Applying cryogenic cooling on the stator surfaces of the ENABLEH2 compressor yielded a core air temperature drop of only 7 K, but without incurring any additional pressure losses for the core air.
 - Only the stator surfaces have been used for heat transfer. There is additional surface area in the hub and shroud of the stators which could also be used for heat transfer.
- Recuperation:
 - Increasing the aspect ratio of the TRS vane or triggering turbulence are measures which increase the overall heat flow, but at a cost of increased core air pressure drop. Combining these two measures increased heat flow by a factor of 3 and the total pressure drop coefficient by 17.5%. This resulted in a core air temperature drop of 2.56 K.
 - As for the ICD there is a need for more surface area to transfer more heat.
- Compact heat exchangers:
 - Compact heat exchangers of the finned tube type have been designed for the ICD and TRS and yield an order of magnitude higher heat flows compared to using the existing aero surfaces.
 - Core air temperature drops between 35 to 50 K can be achieved for the ICD HEX, with effectiveness ranging from 78 to 86% depending on operating point and HEX inlet Mach number. The core air pressure drops ranged from 0.9% to 2.5% while the hydrogen pressure drop was negligible.
 - For the TRS the compact HEX reaches core temperature drops ranging from 140 to 300 K, with effectiveness values from 55 to 92%, also depending on operating point and inlet Mach number. The core air pressure drops ranged from 1.0% to 6.7% while the hydrogen pressure drop was negligible.
 - The most important factor in minimizing the pressure loss in the heat exchanger is to diffuse the flow which decreases its Mach number and dynamic pressure. This then leads to lower pressure losses in the heat exchanger.
 - A large aerodynamic optimization campaign was carried out which optimized the duct shape for an ICD duct consisting of a diffuser, heat exchanger, and contraction. This was carried out for two different area ratios (AR), 4 and 6, and aimed at minimizing the overall total pressure drop of the ducts and minimizing flow non-uniformity at the heat exchanger inlet. It was seen that for well-optimized geometries the largest loss was due to a large incidence angle between the flow and heat exchanger fins. Future modifications of the fin geometry which decreases the incidence will lead to lower losses.
 - Pressure drop correlations were generated from optimized AR4 and 6 ducts and integrated into GESTPAN to be used in engine performance studies.
 - An aluminium alloy has been considered as the structural material for the intercooler and steel for the recuperator, but the final material choices will depend on additional factors such as (but not limited to) mechanical and thermal stresses, operating temperatures, corrosion, and erosion.
- System level performance:
 - Engine performance studies were carried out which integrated compact heat exchangers into the ICD and TRS of the baseline engine model.
 - Performance calculations for an engine featuring an AR 4 *intercooler* have shown an SFC reduction of 1.5-3.0% and EINOx reductions of 12-33% depending on operating point.
 - Performance calculations for an engine featuring an AR 6 *intercooler* have shown an SFC reduction of 2.2-3.4% and EINOx reductions of 16-40% depending on operating point.
 - Performance calculations for an engine featuring an AR 4 *recuperator* have shown an SFC reduction of 5-7% and EINOx reductions of 9-19% depending on operating point.
 - Performance calculations for an engine featuring an AR 4 *intercooler* and an AR 4 *recuperator* have shown an SFC reduction of 5-7% and EINOx reductions of 17-39% depending on operating point. This reduction in fuel consumption is significantly higher than for the intercooling case only, especially at cruise (5% vs 1.5% for this AR).

- The present analysis does not provide the full extent of heat management potential within the hydrogen fuel system. Still, it can be used to set a baseline level for future cycle optimization studies.
- Conceptual designs studies were carried out to determine the impact of intercooling and recuperation on engine architecture and mass. The resulting concepts were evaluated with respect to fuel burn performance using the derived linear trade-factors for the short-medium range aircraft. The highest fuel burn reduction, relative to the baseline, was observed for the recuperated concept, and amounted to 5.1%. The intercooled-recuperated concept, being heavier, resulted in a fuel burn reduction of about 4.8%.
- The intercooled recuperated concept is finally the down-selected configuration. In addition to substantial fuel burn benefit, it achieves reduced core temperatures and the intercooler will also preheat the hydrogen which avoids icing in the recuperator.

7 References

- [1] Document 52019DC0640. Communication From The Commission To The European Parliament, The European Council, The Council, The European Economic And Social Committee And The Committee Of The Regions - The European Green Deal. European Commission. <https://eur-lex.europa.eu/legal-content/EN/TXT/?uri=COM:2019:640:FIN> (accessed May 16, 2022).
- [2] "Data & Statistics - International Energy Agency." <https://www.iea.org/data-and-statistics/data-browser?country=EU28&fuel=CO2emissions&indicator=CO2BySector> (accessed May 16, 2022).
- [3] "Reducing emissions from aviation." https://ec.europa.eu/clima/eu-action/transport-emissions/reducing-emissions-aviation_en (accessed May 16, 2022).
- [4] Arrowsmith, S., D. S. Lee, B. Owen, J. Faber, L. van Wijngaarden, O. Boucher, A. Celikel et al. "Updated analysis of the non-CO₂ climate impacts of aviation and potential policy measures pursuant to the EU Emissions Trading System Directive Article 30 (4)." Cologne, European Union Aviation Safety Agency (EASA) (2020).
- [5] "Trends in Emissions that affect Climate Change." https://www.icao.int/environmental-protection/Pages/ClimateChange_Trends.aspx (accessed May 16, 2022).
- [6] "Strategic Research and Innovation Agenda – 2017 update, Volume 1", Advisory Council For Aviation Research And Innovation in Europe (ACARE)
- [7] Brewer, G. Daniel. Hydrogen aircraft technology. Routledge, 2017.
- [8] Srinath, Akshay Nag, Álvaro Pena López, Seyed Alireza Miran Fashandi, Sylvain Lechat, Giampiero di Legge, Seyed Ali Nabavi, Theoklis Nikolaidis, and Soheil Jafari. "Thermal Management System Architecture for Hydrogen-Powered Propulsion Technologies: Practices, Thematic Clusters, System Architectures, Future Challenges, and Opportunities." *Energies* 15, no. 1 (2022): 304.
- [9] Rolt, A., et al., *Scale effects on conventional and intercooled turbofan engine performance*. The Aeronautical Journal, 2017. 121(1242): p. 1162-1185.
- [10] Xisto, Carlos, Isak Jonsson, and Tomas Grönstedt, "Conceptual Design of a Compressor Vane-HEX for LH₂ Aircraft Engine Applications," no. 769241, p. 769241, 2020.
- [11] Jonsson, Isak, Debarshee Ghosh, Carlos Xisto, and Tomas Grönstedt. "Design of Chalmers new low-pressure compressor test facility for low-speed testing of cryo-engine applications." In *Proceedings of European Conference on Turbomachinery Fluid dynamics*, vol. 14. 2021.
- [12] Jonsson, Isak, Carlos Xisto, Marcus Lejon, Anders Dahl, and Tomas Grönstedt. "Design and pre-test evaluation of a low-pressure compressor test facility for cryogenic hydrogen fuel integration." In *Turbo Expo: Power for Land, Sea, and Air*, vol. 84904, p. V02AT31A022. American Society of Mechanical Engineers, 2021.
- [13] Lejon, Marcus, Tomas Grönstedt, Nenad Glodic, Paul Petrie-Repar, Magnus Genrup, and Alexander Mann. "Multidisciplinary design of a three stage high speed booster." In *Turbo Expo: Power for Land, Sea, and Air*, vol. 50794, p. V02BT41A037. American Society of Mechanical Engineers, 2017.
- [14] Kays, William Morrow, and Alexander Louis London. "Compact heat exchangers." (1984).
- [15] Bergman, Theodore L., Adrienne S. Lavine, Frank P. Incropera, and David P. DeWitt. *Introduction to heat transfer*. John Wiley & Sons, 2011.
- [16] Petukhov, B. S., in T. F. Irvine and J. P. Hartnett, Eds., *Advances in Heat Transfer*, Vol. 6, Academic Press, New York, 1970.
- [17] Gnielinski, Volker. "New equations for heat and mass transfer in turbulent pipe and channel flow." *Int. Chem. Eng.* 16, no. 2 (1976): 359-368.
- [18] Lemmon, Eric W., Ian H. Bell, M. L. Huber, and M. O. McLinden. "NIST standard reference database 23: reference fluid thermodynamic and transport properties-REFPROP, Version 10.0, National Institute of Standards and Technology." *Standard Reference Data Program*, Gaithersburg (2018).
- [19] Bell, Ian H., Jorrit Wronski, Sylvain Quoilin, and Vincent Lemort. "Pure and pseudo-pure fluid thermophysical property evaluation and the open-source thermophysical property library CoolProp." *Industrial & engineering chemistry research* 53, no. 6 (2014): 2498-2508.
- [20] Montero Villar, Gonzalo, Daniel Lindblad, and Niklas Andersson. "Effect of airfoil parametrization on the optimization of counter rotating open rotors." In *AIAA Scitech 2019 Forum*, p. 0698. 2019.
- [21] Montero Villar, Gonzalo, Daniel Lindblad, and Niklas Andersson. "Multi-objective optimization of a counter rotating open rotor using evolutionary algorithms." In *2018 Multidisciplinary Analysis and Optimization Conference*, p. 2929. 2018.
- [22] Patrao, A. Capitaó, G. Montero Villar, J. Takachi Tomita, C. Bringhamti, R. Avellan, A. Lundbladh, and T. Grönstedt. "An optimization platform for high speed propellers." In *Aerospace Technology Congress*. 2016.

- [23]Chen, Po-Shou, and Michael Mitchell. "Alloy NASA-HR-1." Aerospace Structural Metals Handbook (2005).
- [24]Gordon, Sanford, and Bonnie J. McBride. Computer program for calculation of complex chemical equilibrium compositions and applications. Part 1: Analysis. No. NAS 1.61: 1311. 1994.
- [25]Abedi, H., Grönstedt, T., Xisto, C., and Rolt, A. " D2.1 - Heat management system conceptual design tools report." (2018).
- [26]Capitao Patrao, A., B. Gonzalez Lozano, and I. Jonsson. "Numerical modeling of laminar-turbulent transition in an interconnecting compressor duct." In the International Council of the Aeronautical Sciences (ICAS) conference, Stockholm, Sweden, 4-9 September, 2022.
- [27]Varvill, Richard. "Heat exchanger development at Reaction Engines Ltd." Acta Astronautica 66, no. 9-10 (2010): 1468-1474.



ENABLEH2

Public Report

Final report on heat management system

Authors

Alexandre Capitao Patrao, Carlos Xisto, Isak Jonsson, Chalmers University

Anders Lundbladh, GKN



This project has received funding from the European Union's Horizon 2020 research and innovation programme under **grant agreement no 769241**